Mechanisms of the intensification of the upwelling-favorable winds during El Niño 1997–1998 in the Peruvian upwelling system

Adolfo Chamorro Gómez, Vincent Echevin, François Colas, Véra Oerder, Jorge Tam, Carlos Quispe-Ccalluari

Mechanisms of the intensification of the upwelling-favorable winds during El Niño 1997-1998 in the Peruvian Upwelling System

Adolfo Chamorro (1,2), Vincent Echevin (2), Francois Colas (2), Vera Oerder (2,3), Jorge Tam (1), Carlos Quispe-Ccalluari (1)

email: achamorro@imarpe.gob.pe

(1) Instituto del Mar del Perú (IMARPE), Callao, Perú

(2) LOCEAN-IPSL, IRD/CNRS/MNHN/UPMC, UMR7159, Paris, France

(3) Instituto Milenio de Oceanografía (IMO-Chile), Universidad de Concepción, Concepción, Chile

Abstract. The physical processes driving the wind intensification in a coastal band of ~100 km off Peru during the intense 1997-1998 El Niño (EN) event were studied using a regional atmospheric model. A simulation performed for the period 1994-2000 reproduced the coastal wind response to local sea surface temperature (SST) forcing and large scale atmospheric conditions. The model, evaluated with satellite data, represented well the intensity, seasonal and interannual variability of alongshore (i.e. NW-SE) winds. An alongshore momentum budget showed that the pressure gradient was the dominant force driving the surface wind acceleration. The pressure gradient tended to accelerate the coastal wind, while turbulent vertical mixing decelerated it. A quasi-linear relation between surface wind and pressure gradient anomalies was found. Alongshore pressure gradient anomalies were caused by a greater increase in near-surface air temperature off the northern coast than off the southern coast, associated with the inhomogeneous SST warming. Vertical profiles of wind, mixing coefficient, and momentum trends showed that the surface wind intensification was not caused by the increase of turbulence in the planetary boundary layer. Moreover, the temperature inversion in the vertical mitigated the development of pressure gradient due to air convection during part of the event. Sensitivity experiments allowed to isolate the respective impacts of the local SST forcing and large scale condition on the coastal wind intensification. It was primarily driven by the local SST forcing whereas large scale variability associated with the South Pacific Anticyclone modulated its effects. Examination of other EN events using reanalysis data confirmed that intensifications of alongshore wind off Peru were associated with SST alongshore gradient anomalies, as during

the 1997-1998 event.

Keywords

Ocean-atmosphere interactions; Coastal winds; El Niño 1997/1998; Peruvian Upwelling System

1. Introduction

The Peruvian Upwelling System is one of the major upwelling systems of the world in terms of fisheries (Zuta and Guillen 1970; Chavez et al. 2008). A key oceanic process in this nearshore marine environment is the upwelling of deep, nutrient-replete, cold water to the surface forced by Ekman divergence associated with predominantly equatorward coastal winds. As in other upwelling regions, it is characterized by an intense biological productivity (Chavez & Messié 2009) and strong air-sea interactions (e.g. Halpern 2002; Boé et al. 2011; Oerder et al. 2016). A unique aspect of the Peruvian system is its proximity to the equator in the Eastern Pacific, which places it directly under the influence of El Niño events (EN hereafter). During the so called "canonical" EN events, warm surface waters accumulate in the Eastern Tropical Pacific off the Ecuador and Peru coasts (*e.g.* Picaut et al. 2002) causing a dramatic reduction of the upwelling of cold water (*e.g.* Colas et al. 2008). The upwelling reduction is somewhat mitigated by an increase of the equatorward coastal wind (Wyrtki 1975; Kessler 2006). This local wind increase is seemingly paradoxical since large-scale trade winds are weakened in the equatorial (Bjerknes 1966) and subtropical (Rahn et al. 2012) regions. Figure 1a shows the mean spatial distribution of the wind anomalies off Peru coast during the strongest El Niño event observed to date, between November 1997 and February 1998. Positive wind anomalies were maximum onshore and decreased offshore. Negative wind anomalies at the equator indicate the weakening of the southerly trade winds in the equatorial Pacific. The strongest alongshore positive wind anomalies reached ~1.5 m s^{-1} during November 1997-February 1998 which represents a ~40 % increase with respect to the mean climatological conditions (Figure 1b). Note that in the present work, anomalies were computed with respect to mean climatological conditions over the 1994-2000 period.

The processes that drive the nearshore wind increase during EN have not been studied in detail. Previous studies suggested that the wind intensification could be driven by a strengthening of the cross-shore pressure gradient (supporting a geostrophic wind) owing to an enhanced cross-shore thermal contrast between land and sea (Bakun

1990; Bakun et al. 2010). This enhanced thermal contrast would be caused by a stronger temperature increase over land than over sea during EN, due to the greenhouse effect induced by moist air. On the other hand, Enfield (1981) suggested that the enhanced cross-shore thermal contrast during EN was forced by a stronger shortwave heating over land associated with a reduction of nearshore cloudiness. However, SST gradients may also impact on surface winds. Lindzen and Nigam (1987) showed that surface winds over the tropical Pacific can be forced by SST gradients at relatively large scale. Kessler (2006) suggested that the alongshore SST gradient which appears off the Peru coasts during EN may drive a strengthening of the alongshore pressure gradient and wind, but the mechanisms were not studied. In addition, the enhanced atmospheric turbulence due to the surface ocean warming may result in the downward vertical mixing of momentum from the upper layers of the atmosphere to the ocean surface, thus increasing the surface wind (*e.g.* Wallace et al. 1989).

Large scale atmospheric circulation is also impacted by EN, which may affect coastal winds through modifications of the South Pacific Anticyclone (SPA). Dewitte et al. (2011) showed that the alongshore wind intraseasonal (*i.e.* 10-60 days band) variability off central Peru (~15°S) was forced by migratory disturbances across the SPA. Rahn et al. (2012) showed that the SPA was weaker during EN, resulting in decreasing winds off central Chile. Such weakening might mitigate the coastal wind increase during EN off Peru, and a poleward displacement of the SPA might have a similar effect, as shown by Belmadani et al. (2014) in the context of climate change. However, the influence of large-scale atmospheric circulation interannual variability on the coastal winds off Peru remains to be extensively investigated.

In this paper, a regional atmospheric model forced by realistic oceanic (i.e. Sea Surface Temperature) and lateral boundary conditions was used to investigate the physical processes driving the coastal wind intensification during the strong 1997-1998, “eastern pacific” El Niño event. The respective roles of the large scale signal and SST local forcing on the alongshore wind anomalies were also studied for this particular event. Data and methods are described in section 2. Results are presented in section 3, and discussion and conclusions are given in section 4.

2. Data and Methods

2.1 Regional atmospheric model

The Weather Research and Forecasting (WRF) model version 3.3.1 (Skamarock and Klemp 2008) was used to simulate the coastal wind during the period 1994-2000, which includes the very strong 1997-1998 El Niño event (McPhaden 1999). WRF is a fully compressible and nonhydrostatic model. Its vertical coordinate is a terrain-following hydrostatic pressure coordinate. The model uses a time-split integration scheme. Slow and low-frecuency modes are integrated using a Runge-Kutta 3rd order time integration scheme, while the high-frecuency acoustic modes are integrated over smaller time steps to maintain numerical stability. For spatial discretization the model uses a 5th order upwind biased advection schemes. Two nested domains, with one-way offline nesting, were used (Fig.2). The large domain has a resolution of 0.75° and encompasses the South East Pacific and the main part of South America. The small domain has a resolution of 0.25° and covers the Peru and Northern Chile region (30°S-12°N). Both domains include the Andes. The relatively high resolution of the nested domain allows to better represent the orography (Fig. 2), a crucial element of the regional dynamics (e.g. Xue et al. 2004). Both grids have 60 vertical sigma levels between the surface and the top of the atmosphere (defined by the 50 hPa top pressure), with 21 levels in the first ~1000 m. The time steps for the large and nested domains are 180 s and 60 s, respectively.

The parameterizations for short and long wave radiation, cloud physics, land surface and planetary boundary layer (PBL) used in this study are listed in Table 1. Most of them (except the Dudhia (1989) shortwave radiation scheme) are identical to those in the 1/12° configuration of Oerder et al. (2016) for the Peru-northern Chile region. The ERA-interim reanalysis data (Dee et al. 2011), 6-hourly, were used as initial and boundary conditions. The daily Optimum Interpolation Sea Surface Temperature (OISST) at 0.25° (Reynolds et al. 2007) was used as SST forcing. Diurnal SST variations are accounted for in our simulations by using the Zeng and Beljaars (2005) slab model that is included in WRF. Model outputs were recorded every six hours using instantaneous and average values.

2.2 Observational data

Observations from two different satellite-borne scatterometers were used to evaluate the realism of the model surface winds: the ERS weekly wind fields at 1°x1° resolution over the period 1992-2000 and a monthly climatology of QuikSCAT wind fields (hereafter QSCAT) at 1/2°x1/2° resolution grids. The two products were processed by CERSAT (2002a,b) and downloaded from www.ifremer.fr/cersat. Surface winds were interpolated on the 1/4° model grid.

Daily SST and output from ERA-interim reanalysis (see above) were also used in the analysis.

2.3 Monthly momentum budget

In order to investigate the dominant forces that induce the monthly wind changes, we used the following relation demonstrated in Madec (2008; for the NEMO ocean model) and Oerder et al. (2016):

$$\frac{\langle V\rangle - V(t_0)}{\Delta \mathrm{t}} = \sum_{F_n \in \{\mathrm{forces}\}} [F_n] \qquad (1)$$

where $\langle V\rangle$ is the monthly mean wind, $V(t_o)$is the initial velocity at the beginning of the month, $\Delta \mathrm{t}$the time step, and $F_n$the momentum terms: advection $(\vec{v}.\vec{\nabla})\vec{v}$, vertical mixing $\frac{\partial}{\partial z}\left(\frac{\vec{\tau}}{\rho}\right)$, Coriolis $-f\vec{k}x\vec{v}$ and pressure gradient $\frac{-1}{\rho}\vec{\nabla}P$. The bracket ([ ]) is a the double time averaging operator defined as:

$$[F_n] = \frac{1}{\mathrm{N+1}} \sum_{\mathrm{p=0}}^{N} \left(\sum_{\mathrm{k=1}}^{p} F_n\right) \qquad (2)$$

with N the number of time steps during one month.

Based on Eq. (1), we obtain the following relation for two consecutive months (M and M+1):

$$\langle V\rangle_{\mathrm{M+1}} - \langle V\rangle_M = \mathrm{V}(t_{0,\mathrm{M+1}}) - V(t_{0,\mathrm{M}}) + \sum_{F_n \in \{\mathrm{forces}\}} \Delta \mathrm{t} \left([F_n]_{\mathrm{M+1}} - [F_n]_M\right) \qquad (3)$$

On the other hand, a simple integration of the momentum equation between $t_{0,M}$ and $t_{0,M+1}$ (i.e. the respective dates corresponding to the beginning of months M and M+1) leads to:

$$V(t_{0,\mathrm{M+1}}) - V(t_{0,\mathrm{M}}) = \Delta \mathrm{t} \sum_{F_n \in \{\mathrm{Forces}\}} \langle F_n\rangle \qquad (4)$$

Thus $\langle F_n\rangle$ is the time average of the forces between the beginning of the month ($t_{0,M}$) and the beginning of the following month ($t_{0,M+1}$).

Finally, replacing Eq. (4) in Eq. (3), we obtain:

$$\langle V\rangle_{\mathrm{M+1}} - \langle V\rangle_M = \sum_{F_n \in \{\mathrm{forces}\}} \Delta \mathrm{t} \left([F_n]_{\mathrm{M+1}} - [F_n]_M + \langle F_n\rangle\right) \qquad (5)$$

The left side of Eq. (5) represents the change of the monthly mean wind (from month M to month M+1) and the right side represents the sum of the forces contribution. We computed the anomalies of the alongshore (*i.e.* parallel to the WRF model smoothed coastline oriented in the NW-SE direction) component of Eq. (5) (with respect to the “climatology” over 1994-2000, i.e. the average over all years of the difference of one month from its predecessor) in a coastal band of one degree width (4 grid points of the nested domain). This coastal band fully covers the upwelling area which offshore extension is controlled by the shelf topography (Estrade et al. 2008) and does not exceed the Rossby radius of deformation (around 120 km off Peru, e.g. Chavez and Barber 1987). In this area were observed the maximum wind anomalies during the 1997-98 EN (Fig. 1a). WRF code modifications were necessary to save online the individual tendency terms of the momentum balance at each model time step. However modification of the tendency terms due to high-frequency acoustic modes were not saved, which explains why an exact closure of the momentum balance can not be expected.

2.4 Virtual temperature

Virtual temperature is computed in order to estimate the relative contribution of humidity to air density and pressure during EN. The virtual temperature of moist air is the temperature that dry air should have to reach a total pressure and density equal to those of the moist air (Wallace and Hobbs 2006). It is defined by:

$$T_v = \mathrm{T} * (1 + 0.61 * Q_v) \qquad (6)$$

with T the air temperature and Q_v the mixing ratio, which describes humidity.

We computed the monthly virtual temperature anomaly as:

$$T_v' = \left(1 + 0.61 * \overline{Q_v}\right) * \mathrm{T}' + \left(\overline{T} * 0.61\right) * Q_v' \quad (7)$$

with primes marking the monthly anomalies and overlines marking the monthly means. The two terms on the right side of Eq. (7) represent the relative contribution of air temperature and humidity anomalies to the virtual temperature anomaly. Given that virtual temperature is directly proportional to the pressure (for a fixed mass of gas, at a constant volume), these terms contribute to the atmospheric pressure.

2.5 Model simulations

We carried out three experiments with the WRF model. First, a control run was performed over the 1994-2000 period. Then, two experiments (BRY-EN and SST-EN) were performed to isolate the role of the large scale signal from the role of the SST local forcing. The BRY-EN experiment was carried out using the 6-hourly atmospheric boundary conditions from the years 1997-1998 (Niño boundary conditions) and daily SST forcing from the years 1994-1995 (so-called SST neutral conditions) to isolate the role of the large scale signal. The SST-EN experiment was performed using the 6-hourly atmospheric boundary conditions from the years 1994-1995 (neutral boundary conditions) and daily SST forcing from the years 1997-1998 (SST Niño conditions) to isolate the role of the SST local forcing. Note that the 1994-1995 period is considered here as “neutral conditions” for the Peru region as it did not present strong anomalies with respect to climatological conditions, in spite of the occurrence of a weak Central Pacific El Niño in austral spring 1994 and summer 1995.

2.6 Statistical significance

For each of the correlations between two variables presented in the following, the Pearson correlation coefficient (r) was used to measure the strength of a linear association between the variables, and the p-value was used to determine the statistical significance of the relationship.

3. Results

3.1 Validation

3.1.1 Mean and annual cycle of the surface wind

The simulated surface winds were compared with ERS and QSCAT observations. Figures 3 a-c show the annual mean surface wind field obtained from both satellites and the model for the year 2000, when the two satellite observation periods were overlapping. South of the equatorial line, the observed surface winds were strong (~6-8 m s^{-1}) and they blowed north-westward over the oceanic region. They were weaker and approximately parallel to the coastline in the nearshore region, with a maximum (~5-6 m s^{-1}) near 15°S and minimum (~3-4 m s^{-1}) near 18°S (Figs. 3a,c). The model reproduced the observed wind spatial patterns, with a wind intensity closest to that of QSCAT. However, the wind drop-off (*i.e.* wind decrease towards the coast, *e.g.* Capet et al., 2004) was poorly simulated, especially between 10°S and 16°S. It is stronger in QSCAT than in ERS, and both satellites have a blind zone near the coast of approximately 25 km and 50 km respectively where no data are available. Note that wind speed was lower in ERS than QSCAT by ~0.5 m s^{-1} over a large part of the model domain, but that the wind directions were consistent. The differences in wind intensity between ERS and QSCAT are attributed to the use of different operating frequencies, different temporal sampling of the satellites, and gridded products with different spatial resolutions (Bentamy et al. 2013).

Figures 3 d-f show the climatological mean annual cycle of the alongshore wind near the Peru coast. The seasonal cycles were computed over the same time period for ERS and the model (1994-2000), but different time period for QSCAT (2000-2008). The observed alongshore winds were strongest during austral winter (July-

September) and early spring (October) around 15°S. The model wind climatology was in relatively good agreement with the satellite wind climalogies (Pearson's r>0.85, p<0.01). It reproduced the local maximun values (coastal jets) near 4°S and 15°S which are both seen in QSCAT but not in ERS. ERS did not capture the local maximum at 4°S likely due to its lower spatial resolution. The model overestimated the intensity of the alongshore wind with respect to ERS and QSCAT between 3°S and 17°S, and slightly underestimated it with respect to QSCAT in the equatorial region (0-2°S).

3.1.2 Wind and temperature cross-shore vertical structures

The meridional wind and temperature cross-shore vertical structures in the central Peru (at ~15°S) simulated by the model were compared against the ERA-interim reanalysis data (Figure 4). Reanalysis data showed the coastal jet core located a height of ~250 m and within the first 100 km from the coast, with a wind intensity of ~8 m s^{-1} (Fig.4a). The coastal jet is capped by a temperature inversion, which base is located at ~600 m above sea level nearshore. The model reproduced relatively well the intensity of the coastal jet core, although with a position much closer to the coast. In overall, the vertical structures of wind and temperature were well reproduced by the model in the first ~1000 m. Note that the steep topography of the Andes is logically represented with greater detail in the WRF model (Fig. 4b).

3.1.3 Surface winds and SST anomalies during El Niño

The model reproduced the spatial structure of the wind anomalies off Peru (north of ~20°S) during November 1997-February 1998 (Fig. 5a) found in the satellite observations (Fig. 1b). Persistent positive (equatorward) alongshore wind anomalies occured from April 1997 to October 1998 (Fig. 5b) in the 5°S-10°S latitude band. There was a short relaxation period in August 1997 with weak negative anomalies south of 10°S. The strongest positive anomalies (>1.5 m s^{-1}) occured between November 1997 and March 1998. Furthermore, strong negative anomalies (<-1 m s^{-1}) occured in December 1997 - February 1998 north of 5°S. The general pattern of alongshore wind anomalies from the model was consistent with that from ERS (Fig. 1b). However, some discrepancies were found, such as an overestimation of modelled wind anomalies in May-June 1997 and an underestimation in January 1997. Strong SST positive anomalies (>3°C) were seen between May 1997 and May 1998 along the equator in the Eastern Pacific and along the Peru coast (Fig. 5c), with two main peaks (>4°C) between 5°S and 10°S in July-August 1997 and November 1997-April 1998 (Fig. 5d). These peaks were related to the poleward propagation of downwelling coastal-trapped waves, which strongly deepened the thermocline during EN, shutting down the upwelling of cold water (Colas et al., 2008). The amplitude of the SST anomalies slightly reduced in September-October 1997 but remained quite strong (>3°C). Note that although the two SST anomaly peaks were of a relatively similar amplitude, only the second peak was synchronous with strong wind anomalies (> 1.5 m s^{-1}, Fig. 5a) during November 97-April 98, whereas the wind response to the first peak in July-August 1997 was weaker (<1 m s^{-1} in the model and less than 0.5 m s^{-1} in ERS; Fig. 1b). Besides, the model also reproduced the negative wind anomalies north of 5°S between November 1997 and April 1998, a period during which SST anomalies were positive.

3.2 Alongshore momentum budget

First, in order to investigate the spatial patterns of the forces that induced the wind anomalies off Peru during EN, we computed the anomalies of the meridional component of the forces (involved in the meridional monthly momentum budget, see Eq. 5) in the first layer of the model for the whole domain. Each term was then averaged for the period November 1997-February 1998 (Figs. 6a-d). Second, we computed the monthly alongshore anomalies of the forces (i.e. both zonal and meridional components were used in the projection along the NW-SE direction) and averaged them in a coastal band for the entire EN period (Fig. 6e).

Comparison of anomalies of advection, vertical shear of the meridional turbulent stress (hereafter named vertical mixing term), pressure gradient and Coriolis terms shows that pressure gradient and vertical mixing were the dominant forces (Figs. 6b,c). The pressure gradient anomaly was positive (Fig. 6c), thus accelerated the equatorward wind during EN. Expectedly, vertical mixing anomaly was opposed to the equatorward wind thus negative (Fig. 6b). The two terms almost balanced each other everywhere in the domain, except in the region between 0-5°S where advection anomaly was relatively strong (Fig. 6a) and pressure gradient and vertical mixing anomalies were much weaker. Coriolis term anomalies had much smaller values (Fig. 6d).

Figure 6e shows the time evolution of the monthly anomalies of the surface forces projected in the alongshore direction. The terms were averaged in a one-degree-wide coastal band between 7°S and 15°S (this coastal region was chosen because the coastline is relatively rectilinear and the wind anomalies were relatively homogeneous in space). The pressure gradient and vertical mixing were the main forces during the entire time period. The dates corresponding to pressure gradient maximum (positive anomalies) values coincided with those of vertical mixing minimum (negative anomalies) values (*e.g.* in June-July and November-December 1997 and April-May 1998). The advection term was weaker, except in July-September and October-November 1997. The contribution of the Coriolis force was negligible during the entire period. The tendency ($\Delta V'$: month to month wind anomaly difference) was almost equal to the sum of all terms, showing that the budget (see Eq. (5) in section 2.3) is virtually closed. The small differences in the budget (RMS error of ~6% over the simulation period) come from the acoustic correction (see sections 2.1 and 2.3).

The wind intensification during EN occurred during different phases (Fig. 6e, dashed-black line). It began in March 1997 ($\Delta V'$~1 m s^{-1} from March to April 1997) and was maintained until June 1997, due to a positive equatorward pressure force stronger than the sum of the other (negative) terms. The wind anomaly then strongly decreased ($\Delta V'$~-1.2 m s^{-1} from June to July 1997) due to a negative advection of momentum between June and August 1997, which was related to the large scale forcing. A similar momentum budget for the BRY-EN experiment confirmed this large scale modulation (figure not shown). The wind acceleration became strong again in September 1997 ($\Delta V'$~1.5 m s^{-1} from September to October), when advection weakened and the pressure gradient dominated the other forces. The tendency was weak from January to May 1998. In the later phase of EN, the wind anomaly was strongly reduced from May to July 1998, due to a decrease of the pressure gradient.

Consistently with previous studies (Muñoz and Garreaud, 2005; Belmadani et al., 2014), alongshore pressure gradient anomalies were highly correlated (r=0.8, p<0.01) with alongshore wind anomalies averaged over the coastal band (line red and dashed-black line in Fig. 6e). Although it displays smaller spatial scales than the alongshore wind, the pressure gradient explains relatively well the wind intensification between 5°S and 16°S during the peak of EN but also over limited portions of the coast in June 1997 and August 1998 (Fig.7a). More specifically, a strong correlation (r=~0.75, p<0.01) between alongshore pressure gradient anomalies and alongshore wind anomalies was found along the coast for latitudes between 4°S and 18°S (Fig. 7b). In this sense, on average over a coastal band (7°S-15°S) ~64% of the temporal variability of the wind anomalies was explained by pressure gradient anomalies, suggesting that vertical mixing behaved like a linear bottom frictional term equilibrating the pressure gradient. This led to the following relation $V = \frac{-1}{c\rho}\frac{\partial P}{\partial y}$ with c the linear friction coefficient and ρ the surface air density. From our model results, c was ~ 4 10^{-5} s^{-1}, thus comparable to Muñoz and Garreaud (2005)'s estimation for the Chile central coast (c ~ 5 10^{-5} s^{-1}). The steep orography of the Andes precluded the development of an anomalous cross shore flow, thus the alongshore pressure gradient can not be equilibrated by the Coriolis force. Consequently the alongshore flow built up until the frictional force (i.e. vertical mixing term) balanced the alongshore pressure gradient.

In summary, the pressure gradient term played a major role in initiating and terminating the wind anomaly during this EN event. In the next sections we study in detail the processes that drive the pressure gradient increase at the beginning of the event.

3.3 Air temperature and humidity contributions to the alongshore pressure gradient

As surface pressure is related to virtual temperature in the air column (see Section 2.4), we examined the relative contributions of temperature and humidity anomalies to the virtual temperature anomalies (VTA) (see Eq. (7) in section 2.4) during EN (November 1997-February 1998). The VTA distribution displayed the largest positive anomalies (>4 °K) along the north coast between 4°S and 8°S and in the lowest 300 m (Fig. 8a). Temperature variations dominated VTA (Fig. 8b), while humidity anomalies contributed to at most ~15% of the VTA (north coast around 400 m, Fig.8c). The humidity anomaly was stronger at 400 m because humidity was higher and nearly constant from the surface up to ~400 m before decreasing progressively with altitude during EN, whereas it progressively decreased with altitude with a relatively constant vertical gradient from the surface to 900m under mean climatological conditions (Fig. 8d). These results show that the stronger temperature increase in the north of Peru was the main driver of the alongshore pressure gradient anomaly during the EN event, while humidity did not play an important role.

This thermally driven pressure gradient was confirmed by the high correlation ($r=0.84$, $p<0.01$) between the surface wind anomaly in the coastal band and the alongshore SST gradient (Fig. 9). This correlation was slightly higher (0.87) with a 1 month lag (when the SST gradient leads the wind). This suggests that the anomalously warm surface ocean forced the low atmosphere by heating the air column more in the north than in the south, thus generating the pressure gradient that drove the equatorward wind anomaly.

3.4 Downward mixing of momentum during EN

Due to the air warming and humidification associated with the presence of anomalously warm surface waters in the nearshore region, shallow convection was enhanced. In the coastal band, the planetary boundary layer height (PBLH) increased by ~200 m (~50%) around June 97 and by ~100-150m (~100%) between December 1997-March 1998 (Fig. 10). The PBLH increases were in phase with the SST anomalies peaks, and slightly stronger in the north than in the south, in agreement with the SST spatial changes (not shown).

Given this PBL variability, a potential mechanism for the wind intensification could be associated with the increase of turbulence in the PBL during EN, which may generate a more efficient downward vertical flux of momentum (Wallace et al. 1989). However, turbulent mixing tended to decelerate the wind even more during the warm EN phases (Fig. 6e). To further investigate why Wallace et al. (1989)'s mechanism can not explain the EN wind increase, we examined the vertical profiles of alongshore wind, turbulent vertical mixing coefficient, momentum budget forces contribution, and temperature during climatological and EN conditions in November 1997-February 1998 (Fig. 11). The wind intensification during EN occurred between the sea surface and ~1600 m (black line in Fig. 11a). The wind maximum (~8 m s^{-1}) shifted from ~300 m in mean climatological conditions to ~500 m. There was a decrease of wind shear (dV/dz) below ~500m during EN, mainly due to the velocity increase at the surface (~20%) and a virtually unchanged velocity at 300 m (black line in Fig. 11a). Turbulent vertical mixing coefficient (K_z) increased almost twofold during EN reaching a maximum of ~40 $m^2.s^{-1}$ at 200 m (~15 m^2 s^{-1} in climatological conditions, blue line in Fig. 11a). The impact on the turbulent stress (τ=K_z.dV/dz) of the wind shear decrease and turbulent vertical mixing (K_z) increase was such that the momentum vertical mixing term (dτ/dz) reduced (it is negative in mean climatological conditions, blue line in Fig 11b and 12b) during EN conditions (Fig. 6e; blue line in Fig. 11c). This also shows that the EN wind intensification near the surface was not driven by downward mixing of momentum. The pressure gradient (positive in mean climatological conditions, red line in Fig. 11b and 12b) increase was maximum at the surface and decreased with height during EN conditions (red line in Fig. 11c). The Coriolis and advection terms did not change much during EN (magenta and green lines in Fig. 11c), but they are relatively important for the budget in mean climatological conditions (magenta and green lines in Fig. 11b and 12b). Note that the pressure gradient was strong at surface and in upper layers during EN. Air temperature decreased between the surface and 1600 m, showing no temperature inversion in this period (austral summer) in mean climatological or EN conditions (Fig. 11d).

This time period is contrasted with the period July-August 1997, during which the surface wind anomalies were weak (Figs. 5a and 12a) in spite of SST anomalies of the same order (~4°C) as during November 1997-April 1998 (Fig. 5b). Between the surface and 800 m the wind speed decreased with respect to mean climatological conditions, and did not change in the upper layers (800-1600m). The wind shear decreased between the surface and 400m (black line in Fig. 12a), mainly due to the velocity decrease between 300-400 m (~10%) and a virtually unchanged velocity at surface. Mixing coefficient (K_z) increased by almost 70% in this period, reaching a maximum of ~74 $m^2.s^{-1}$ at 250 m (~45 m^2 s^{-1} in climatological conditions at 220 m, blue line in Fig. 12a). The changes in wind shear and turbulent vertical mixing (K_z) in this period counteracted such that the momentum vertical mixing term did not change significantly (blue line in fig 12c), thus compensation . The wind decrease below ~600 m was likely driven by advection, which decreased below 500 m (green line in Fig. 12c) whereas the pressure gradient change remained positive (red line in Fig. 12c). On the other hand, the pressure gradient vertical shear between the surface and ~600 m (Fig. 12c) was stronger than in November 1997-February 1998 period (Fig. 11c). Note also the well-marked temperature inversion in July-August 1997 (Fig. 12d). The effect of this particular vertical structure on the pressure gradient will be discussed below (Sect. 4.2).

3.5 Impacts of large scale atmospheric forcing and local SST forcing

In this subsection, we analyzed the model sensitivity experiments to study the respective roles of the large scale atmospheric signal (BRY EN experiment, forced by 1997-1998 EN boundary conditions and neutral SST forcing from the years 1994-1995) and of the SST local forcing (SST-EN experiment, forced by EN SST forcing and 1994-1995 neutral boundary conditions, see section 2.5) in driving the EN wind anomalies.

Figure 13a displays the alongshore surface wind anomalies (averaged in the coastal band between 7°S and 15°S) for the CRTL, BRY-EN, SST-EN experiments. The large scale signal (BRY-EN simulation) during EN induced strong negative wind anomalies (~ -1 m s^{-1}) between March and September 1997, and moderate (<1 m s^{-1}) positive anomalies between October 1997 and March 1998. In contrast, the model forced by the 1997-98 SST forcing (SST-EN) simulated persistent positive wind anomalies between May 97 and August 97 (reaching ~1 m s^{-1} in August 97) and between November 1997 and May 1998 (peaking at ~1.5 m s^{-1} in January-February 98). There was a slightly negative anomaly in September 1997, which coincided with the slight decrease of SST anomaly in September-October 1997 (Fig. 5b). Note that the wind anomaly was negligible in CRTL in Jul-Aug

1997, in spite of a strong SST anomaly (~3-4 °C, Fig. 5b). This can be explained by the large scale signal, which forced a decrease of the equatorward wind (negative anomalies of ~ -1 m s^{-1} in July-September 1997 in BRY-EN) which compensated the wind increase (~ 0.5-1 m s^{-1} in SST-EN) forced by the anomalously warm SST.

In the first warm period (July-August 1997), the intensification of the wind driven by the SST forcing (SST-EN experiment) was compensated by the large scale signal (BRY-EN) not only at the surface but also as high as 1400 m (Fig. 13b). During the second period (November 1997-February 1998), boundary conditions (BRY-EN simulation) did not have a strong effect. The wind was modified very little in the vertical with respect to climatological conditions. The wind intensification below 200 m was fully forced by the anomalous SST (Fig. 13c).

Thus, the BRY-EN experiment showed that the large-scale atmospheric signal propagating into the Peru region through the open boundaries could mitigate (or enhance) the coastal wind anomalies during EN. The SPA center was located around its mean climatological position into both periods (red lines in Figs 14 a,b). However, during March–September 1997, the SPA was weaker (-1-2 hPa anomaly) than in mean climatological conditions (Fig.14a). This weakening should produce negative anomalies for the surface atmospheric pressure off Peru, which likely contributed to a decrease of the alongshore wind off Peru in the BRY-EN simulation. Indeed, the maximum surface pressure in the SPA was well correlated (0.67) with BRY-EN wind anomalies during the EN period. In contrast with the March-September 1997 period, the SPA was slightly more intense in October 1997–March 1998 (Fig. 14b) and September 98 (not shown), favoring an intensification of the coastal wind during these time periods due to SST forcing (Fig.13a).

4. Discussion and conclusions

4.1 Summary

A regional atmospheric model was used to investigate the physical processes driving the wind intensification off the Peru coast during the 1997-1998 EN event. As anomalously warm waters accumulated near the coast, the equatorward coastal wind increased by ~1-1.5 m s^{-1} during 5-6 months (up to ~40 % increase with respect to the climatological mean over the 1994-2000 period). Simulated surface wind anomalies during EN were in good agreement with observed wind anomalies. A momentum balance analysis showed that the coastal wind intensification was mainly driven by the enhancement of the alongshore pressure gradient. Vertical mixing tended to counterbalance the alongshore pressure gradient, leading to a quasi-equilibrium between the alongshore pressure gradient and the frictional force, consistently with previous modeling studies in the region (Muñoz and Garreaud, 2005; Belmadani et al., 2013). The enhancement of the alongshore pressure gradient occured because the atmospheric pressure decreased more north (~6°S) than south (~14°S), in association with the larger increase of SST, air temperature and humidity off northern Peru. Surface warming induced an increase of the height of the PBL of up to two and half times and of the vertical turbulent mixing coefficient ($K_z=\tau/(dV/dz)$) of up to three times their values in mean climatological conditions. However vertical mixing of momentum ($d\tau/dz$) remained negative and was stronger (in absolute value) during EN that in mean climatological conditions, thus did not accelerate the equatorward wind.

4.2 The back-pressure effect during EN

The alongshore pressure gradient change was strong at surface and its vertical structure varied during the EN period: the pressure gradient change was strong between the surface and ~1000m when there was no temperature inversion (*e.g.* in November 1997-February 1998; Figs. 11b,c). In contrast, it became negligible above 600m in the presence of a marked temperature inversion (*e.g.* in July-August 1997; Figs. 12b,c). Hashizume et al. (2002) showed that the so-called “back-pressure effect”, a mechanism compensating the surface pressure gradients, was strong in the case of a marked temperature inversion above the PBL. Oerder et al. (2016) found that this effect reduced significantly the intensity of the surface pressure gradient above mesoscale SST positive anomalies in the Peru region. This is also likely the case in the Peru coastal region in our simulation during the period July-August 1997 (Fig. 12c). Note that temperature inversion is related to the strong atmospheric subsidence in the region led by the SPA (e.g. Haraguchi 1968).

In conclusion, it is likely that two conditions, a SST anomaly alongshore gradient and a weak (or absent) temperature vertical inversion would be necessary to drive a strong surface wind anomaly in the coastal region. The SST gradient drives the pressure gradient, and the weak temperature inversion allows shallow convection to develop without triggering any “back-pressure effect”.

4.3 Land-sea thermal contrast

Bakun et al. (2010) suggested that the increase of humidity over coastal land during EN could enhance the local greenhouse heating effect, thus increasing land temperature more than SST. This thermal contrast would lead to the presence of lighter air over land than over sea, an intensification of the cross-shore pressure gradient and associated alongshore geostrophic wind. Similarly, Enfield (1981) suggested that a land-sea thermal contrast may occur due to an increase of downward solar radiation over land, which would be due to a reduction of cloudiness during EN. As Bakun et al. (2010) and Enfield (1981) suggested, humidity and incoming solar radiation increased over land during EN in our simulations (green and red lines respectively; Fig. 15). However, this increase in humidity and short wave radiation reaching the land surface did not support a strengthened land-sea thermal contrast. Indeed, the simulated land-sea contrast, which was positive (*i.e.* air temperature was higher over land than over sea) in mean climatological conditions (not shown), decreased by ~100% during EN (blue line in Fig.15) as the air temperature over sea increased much more than the air temperature over land (not shown). Note that a clear relation between land-sea thermal contrast and alongshore winds off Peru has not been demonstrated in previous studies. Using a set of GCM simulations with a spatial resolution of ~50 km in the Peru-Chile region, Belmadani et al. (2013) found that the land-sea thermal contrast (dT/dx) increased off Peru in scenarios of climate change: at 8°S, dT/dx was ~4.5 10^{-2} K km^{-1} in preindustrial climate conditions, and reached ~6.5 10^{-2} K km^{-1} in 4xCO_2 climate conditions, thus increased by ~40% (see Figure 8c in Belmadani et al. 2013). In spite of this strong increase, the alongshore wind decreased moderately (~10%) off Peru. This reduction was driven by a decrease of the alongshore pressure gradient associated with a poleward displacement of the SPA in a warmer climate (Belmadani et al. 2013 and references herein). This and our results suggest that an increase of the land-sea thermal gradient may not play a strong dynamical role for the alongshore wind, at least for the range of horizontal resolution (~25 km in the present study and ~50 km in Belmadani et al. 2013) explored in our model simulations. Note that these resolutions do not allow to represent the coastal terrain located between the Andes and the ocean with more than a few grid points.

In addition, our model simulated poorly the mean downward shortwave radiation associated with the cloud cover, a well-known problem in models of the Southeast Pacific lower troposphere (e.g. Wyant et al. 2010). Despite this bias, the model reproduced reasonably well the surface air temperature distribution and, more importantly for the purpose of the present study, the air temperature anomalies at surface during EN, in agreement with reanalysis data (not shown). The modelled air temperature increased more over sea than over the land during EN associated with the strong SST warming, thus reducing the land-sea thermal contrast. However, the land-sea thermal contrast may impact the wind at scales smaller than those resolved by the present model (e.g. Enfield, 1981). This process remains to be investigated using higher resolution model experiments in future work.

4.4 Dynamical processes during other EN events

Due to the model computational cost, our simulations were performed for a relatively short time period (1994-2000) including only one EN event. In order to evaluate if the same dynamical processes were active during other events, we performed similar diagnostics using the ERA-Interim reanalysis data over the period 1979-2016. This data has a lower spatial resolution (~80 km) than our regional model, but it can give hints of the processes at stake during EN events. The wind anomaly (in a coastal band of ~160 km and between 7°S and 15°S) for the 1997-98 EN was ~0.6-0.8 m s^{-1}, less than in our model (~1.0-1.2 m s^{-1} for an average over 6 WRF grid points). We found relatively strong wind anomalies during most EN events, in particular in 1982-83 (~0.8 m s^{-1}), 1987-88 (~1 m s^{-1}), 1992-93 (0.7 m s^{-1}), 2015-16 (0.8 m s^{-1}) (Fig. 16). In agreement with our analysis, these four events were associated with positive alongshore SST gradient anomalies (*e.g.* ~0.15 10^{-2} °C km^{-1} in 1982-83). There were also EN events with relatively weak wind anomalies (i.e. 2002-2003). Note that strong SST gradient anomalies occurred during relatively short time periods in 1993, 2002 and 2008, and were not associated with positive wind anomalies. We may conjecture that other processes such as a compensation by the large scale forcing through a modification of the SPA or the presence of temperature inversion with a back-pressure effect may be active during these periods.

4.5 Local air-sea coupled processes during EN

Local air-sea coupled interactions not investigated in the present study may also play a role during EN. First, the increase of humidity in the north of Peru leads to intense precipitation on land and over the nearshore ocean (Takahashi, 2004), which may enhance the ocean surface stratification. This may mitigate wind-driven oceanic vertical mixing in the north and thus help maintaining the anomalous alongshore SST gradient driving the coastal wind. On the other hand, the stronger coastal wind (Figs 1b and 5a), SST (Fig.5b) and humidity (Fig.8c) anomalies in the north would increase evaporation and thus cool the ocean more efficiently than further south. This effect may mitigate the SST gradient and thus reduce the wind anomaly. Studying such feedbacks, which were not taken into account in our forced atmospheric model framework, is beyond the scope of the present study. These questions, which can be addressed using a regional high resolution, ocean-atmosphere coupled model (*e.g.* Oerder at al. 2016), will be the purpose of future studies.

5. **Acknowledgments**

This research is part of A. Chamorro's PhD thesis, funded by the fellowship from CIENCIACTIVA/CONCYTEC-PERU at the University Pierre and Marie CURIE of France. It is also part of the IDB project PE-G1001(Adaptation to Climate Change of the Fishery Sector and Marine-Coastal Ecosystem), and it is a contribution to the cooperative agreement between the Instituto del Mar del Peru (IMARPE) and the Institut de Recherche pour le Developpement (IRD) and the LMI DISCOH. The simulations were performed on the supercomputer Curie from the GENCI at the CEA (projects 2011040542, 2012061047 and 2014102286). Francois Pinsard is acknowledged for her help in the making of lateral boundary forcing for the regional atmospheric model. Francis Codron and Clémentine Junquas are acknowledged for useful discussions.

6. References

Bakun A, Field D, Renondo-Rodriguez A, Weeks SJ (2010) Greenhouse gas, upwelling favourable winds, and the future of upwelling systems. Glob Chang Biol 16:1213-1228

Belmadani A, Echevin V, Codron F, Takahashi K, Junquas C (2014) What dynamics drive future wind scenarios for coastal upwelling off Peru and Chile? Clim Dyn 43: 1893-1914. doi:10.1007/s00382-013-2015-2

Bentamy A, Grodsky SA, Katsaros K, Mestas-Nuñez AM, Blanke B, Desbiolles F (2013) Improvement in air-sea flux estimates derivedfrom satellite observations. Int J Remote Sens 34(14):5243–5261. doi:10.1080/01431161.2013.787502

Bjerknes J (1966) Survey of El Niño 1957-58 in its relation to tropical Pacific meteorology. Inter-American Tropical Tuna Commission Bulletin 12(2):, pp 1-62

Boé J, Hall A, Colas F, McWilliams JC, Qu X, Kurian J, Kapnick SB (2011) What shapes mesoscale wind anomalies in coastal upwelling zones? Clim Dyn 36(11–12):2037–2049

Capet XJ, Marchesiello P., McWilliams JC (2004) Upwelling response to coastal wind profiles. Geophys Res Lett 31, L13311. doi:10.1029/2004GL020123

Carr M-E., Strub PT, Thomas AC, Blanco JL (2002) Evolution of 1996 – 1999 La Nina and El Nino conditions off the western coast of South America: A remote sensing perspective. J Geophys Res 107(C12), 3236. doi:10.1029/2001JC001183

CERSAT (2002a) Mean wind fields (MWF product) user manual volume 1: ERS-1, ERS-2 & NSCAT. Rep C2-MUT-W-05-IF. CERSAT-IFREMER, Brest

CERSAT (2002b) Mean wind fields (MWF product) user manual volume 1: QuikSCAT. Rep C2-MUT-W-04-IF. CERSAT-IFR- EMER, Brest

Chavez FP, Barber RT (1987) An estimate of new production in the equatorial Pacific. Deep-Sea Research 34(7):1229-1243. doi.org/10.1016/0198-0149(87)90073-2

Chavez FP, Bertrand A, Guevara-Carrasco R, Soler P, Csirke P (2008) The northern Humboldt Current System: Brief history, present status and a view towards the future. Prog Oceanogr 79(2–4):95-105. doi:10.1016/j.pocean.2008.10.012

Chavez FP, Messié M (2009) A comparison of eastern boundary upwelling ecosystems. Prog Oceanogr 83(1):80-96.

Chen F, Dudhia J (2001) Coupling an advanced land surface hydrology model with the penn state-NCAR MM5 modeling system. Part ii: Preliminary model validation. Mon Weather Rev 129(4):587–604. doi:10.1175/1520-0493(2001)129<0587:CAA LSH>2.0.CO;2

Colas F, Capet X, McWilliams JC, Shchepetkin A (2008) 1997–98 El Niño off Peru: A numerical study. Prog

Oceanogr 79:138-155. doi:10.1016/j.pocean.2008.10.015.

Dee, D.P. et al (2011) The ERA-Interim reanalysis: configuration and performance of the data assimilation system. Q J R Meteorol Soc A 137:553–597. doi:10.1002/qj.828

Dudhia J (1989) Numerical study of convection observed during the winter monsoon experiment using a mesoscale two-dimensional model. J Atmos Sci 46:3077-3107. doi:10.1175/1520-0469(1989)046<3077: NSOCOD>2.0.CO;2.

Enfield DB (1981) Thermally-driven wind variability in the planetary boundary layer above Lima, Peru. J Geophys Res 86(C3):2005-2016

Estrade P, Marchesiello P, Colin de Verdiere A, Roy C (2008) Cross-shelf structure of coastal upwelling: A two-dimensional expansion of Ekman’s theory and a mechanism for innershelf upwelling shut down. J Mar Res 66:589-616.

Haraguchi PY (1968) Inversions over the tropical eastern Pacific ocean. Mon Weather Rev 96:177–185

Hashizume H, Xie SP, Fujiwara M, Tanimoto TWY (2002) Direct observations of atmospheric boundary layer response to SST variations associated with tropical instability waves over the Eastern Equatorial Pacific. J Clim 15:3379–3393. doi:10.1175/1520-0442(2002)015<3379:DOOABL>2.0.CO;2

Hong S, Lim J (2006) The WRF single-moment 6-class microphysics scheme (WSM6). J Korean Meteorol Soc 42(2):129–151

Janjic ZI (1994) The step-mountain eta coordinate model: further developments of the convection, viscous sublayer, and turbulence closure schemes. Mon Wea Rev 122:927–945. doi:10.1175/1520-0493(1994)122<0927:TSMECM>2.0.CO;2

Kessler WS (2006) The circulation of the eastern tropical Pacific: A review. Prog Oceanogr 69(2):181-217

Lindzen R, Nigam S (1987) On the role of sea surface tem- perature gradients in forcing low level winds and convergence in the Tropics. J Atmos Sci 44:2418–2436. doi:10.1175/1520-0469(1987)044<2418:OTROSS>2.0.CO;2

Nakanishi M, Niino H (2009) Development of an improved turbulence closure model for the atmospheric boundary layer. J Meteorol Soc Jpn 87:895–912. doi:10.2151/jmsj.87.895

Madec G (2008) NEMO ocean engine. Note du Pole de modélisation, Institut Pierre-Simon Laplace (IPSL) 27. ISSN No. 1288–1619.

McPhaden MJ (1999) Genesis and evolution of the 1997–98 El Niño. Science 283:950-954.

Mlawer E, Taubman S, Brown P, Iacono M, Clough S (1997) Radiative transfer for inhomogeneous atmosphere: RRTM, a validated correlated-k model for the long-wave. J Geophys Res 102:16,663–16,682. doi:10.1029/97JD00237

Muñoz RC, Garreaud RD (2005) Dynamics of the low-level jet off the west coast of subtropical South America. Mon Wea Rev 133:3661–3677. doi:10.1175/MWR3074.1

Oerder V, Colas F, Echevin V, Masson S, Hourdin C, Jullien S, Gurvan M, Lemarié F (2016) Mesoscale SST-wind stress coupling in the Peru-Chile current system: Which mechanisms drive its seasonal variability? Clim Dyn (2016) 47:2309. doi:10.1007/s00382-015-2965-7

Penven P, Echevin V, Pasapera J, Colas F, Tam J (2005) Average circulation, seasonal cycle, and mesoscale dynamics of the Peru current system: Amodeling approach. J Geophys Res 110, C10021. doi:10.1029/2005JC002945

Picaut J, Hackert E, Busalacchi A, Murtugudde R , Lagerloef GSE (2002), Mechanisms of the 1997–1998 El Niño–La Niña, as inferred from space-based observations. J Geophys Res Oceans 107 (C5). doi: 10.1029/2001JC000850.

Rahn DA (2012) Influence of large scale oscillations on upwelling-favorable coastal wind off central Chile. J Geophys Res 117, D19114. doi:10.1029/2012JD018016

Renault L, Hall H, McWilliams JC (2016) Orographic shaping of USWest Coast wind profiles during the upwelling season. Clim Dynam 46:273–289. doi:10.1007/s00382-015-2583-4

Reynolds RW, Smith TM, Liu C, Chelton DB, Casey KS, Schlax MG (2007) Daily high-resolution-blended analyses for sea surface temperature. J Climate 20:5473-5496. doi:10.1175/2007JCLI1824.1.

Skamarock W, Klemp J (2008) A time-split nonhydrostatic atmos- pheric model for weather research and forecasting applications. J Comp Phys 227:3465–3485. doi:10.1016/j.jcp.2007.01.037

Strub PT, J Mesías, V Montecino, J Rutllant & S Salinas. 1998. Coastal ocean circulation off Western South America. In: Robinson AR & KH Brink (eds). The global coastal ocean: Regional studies and syntheses. The Sea 11: 273-314. John Wiley, New York.

Takahashi K (2004) The atmospheric circulation associated with extreme rainfall events in Piura, Peru, during the 1997-1998 and 2002 El Niño events. Ann Geophys 22:3917-3926. doi:10.5194/angeo-22-3917-2004

Takahashi K, Battisti DS (2007) Processes Controlling the Mean Tropical Pacific Precipitation Pattern. Part I: The Andes and the Eastern Pacific ITCZ. Journal of Climate 20:3434-3451. doi: 10.1175/JCLI4198.1

Wallace JM, Hobbs PV (2006) Atmospheric Science: A Introductory Survey. 2nd ed. Academic Press, pp 483

Wallace JM, Mitchell T, Deser C (1989) The influence of sea surface temperature on surface wind in the Eastern

Equatorial Pacific: seasonal and interannual variability. J Clim 2:1492–1499. doi:10.1175/1520-0442(1989)002<1492:TIOSST>2.0.CO;2

Wyant MC et al (2010) The PreVOCA experiment: modeling the lower troposphere in the Southeast Pacific. Atmos Chem Phys 10:4757–4774. doi:10.5194/acp-10-4757-2010

Wyrtki K (1975). El Niño: the dynamic response of the equatorial Pacific to atmospheric forcing. Journal of Physical Oceanography 5:572–584

Xue H, Wang Y, Xie SP (2004) Effects of the andes on eastern pacific climate: a regional atmospheric model study. J Clim 17:587–602

Zeng X, Beljaars A (2005) A prognostic scheme of sea surface skin temperature for modeling and data assimilation. Geophysical Research Letters 31:L14605. doi: 10.1029/2005GL023030

Zuta S, Guillén O (1970) Oceanografía de las aguas costeras del Perú. Boletin Instituto del Mar del Perú 2: 157–324

7. Tables

Table 1. Parameterizations used in WRF model for the simulations.

Processes	Scheme	Reference
Shortwave Radiation	Dudhia scheme	Dudhia (1989)
Longwave Radiation	RRTM scheme	Mlawer et al. (1997)
Microphysics	WRF Single-Moment 6-class scheme	Hong and Lim (2006)
Cumulus	Betts-Miller-Janjic scheme	Janjic (1994)
Surface Layer	MYNN surface layer	Nakanishi and Niino (2009)
Land Surface	Noah Land Surface Model	Chen and Dudhia (2001)
Planetary Boundary Layer	MYNN Level 2.5 PBL	Nakanishi and Niino (2009)

8. Figure captions

Figure 1. a) ERS wind anomalies (in m s^{-1}) off Peru and Northern Chile during El Niño conditions in November-February 1997/1998. Arrows mark the direction of the monthly wind anomalies. b) Time-latitude diagram of ERS alongshore monthly wind anomalies off the Peru coast. The wind average was computed within a 100 km-wide coastal band and a 3-month running mean was applied. Positive values indicate equatorward wind anomalies.

Figure 2. South East Pacific model domain and Peru nested domain used in the WRF simulations. Color shading indicates model topography (in meters) above sea level for the small domain.

Figure 3. Mean surface wind (in m s^{-1}) in 2000 from a) ERS satellite, b) WRF model and c) QSCAT satellite. Mean annual cycle of the alongshore wind (averaged in a 100-km-wide coastal domain) from d) ERS and e) WRF over the period 1994-2000, and from f) QSCAT over the period 2000-2008.

Figure 4. Vertical structure of the mean meridional wind (shading, in m s^{-1}) and air temperature (black contours, in °C) at 15°S from a) ERA-Interim and b) WRF model. Data was averaged for the 1994-2000 period.

Figure 5. a) Mean surface wind anomalies (in m s^{-1}) from WRF (over November 1997-February 1998) and b) time-latitude diagram of WRF alongshore wind anomalies. c) Mean sea surface temperature (SST) anomalies (in °C) from OISST (over the same time period in a)) and d) time-latitude diagram of alongshore SST anomalies.

Figure 6. Anomalies of the meridional component of the surface forces contribution (in m s^{-1}) during El Niño 1997/1998: a) advection (V-ADV'), b) vertical turbulent mixing (V-MIX'), c) pressure gradient (V-PGF'), and d) Coriolis force (V-COR'). Anomalies were computed with respect to a climatology over 1994-2000 and averaged over November 1997-February 1998. e) Time series of the monthly anomalies of the alongshore component of the surface forces contribution in 1997-1998 (in m.s^{-1}, with scale defined by the left-hand side y axis). The forces were averaged in a 100-km coastal band between 7°S and 15°S. Gray, black and black-dashed lines

indicate tendency (the month to month wind anomaly difference), the sum of all terms and wind anomaly (relative to climatology), respectively (in $m.s^{-1}$, with scale defined by the right-hand side y axis).

Figure 7. a) Alongshore anomalies of pressure gradient (in m s^{-1} , shading) and coastal wind (in m s^{-1}, black contours) between the equator and 20°S. b) Latitudinal variation of the correlation between alongshore pressure gradient anomalies and alongshore coastal wind anomalies.

Figure 8. Alongshore vertical sections of the mean monthly anomalies (during November 1997-February 1998) of a) virtual temperature (in °C) and b) temperature and c) humidity contributions (in °C) to the virtual temperature anomaly. Note the different scales for temperature and humidity contribution. d) Vertical profiles of humidity in the northern coastal region (4°S-8°S) during November 1997-January 1998 (full line) and mean climatological conditions (dashed line).

Figure 9: Time evolution of alongshore SST gradient (in °C/25km, positive equatorward, red line) and wind (in m s^{-1}, black line) anomalies. Anomalies were smoothed using a 3-month running mean, and averaged between 7°S and 15°S and within 100 km from the coast.

Figure 10. Mean Planetary Boundary Layer Height (in meters, PBLH) off Peru. PBLH was averaged between 7°S and 15°S and within 100 km from the coast. Red line marks PBLH during 1997-1998, and black dashed line the climatology. Error bars indicate standard deviation from the mean climatological values.

Figure 11. Vertical profiles of a) alongshore wind (in m s^{-1}), b) alongshore forces in mean climatological conditions (in m s^{-1}), c) anomalies of alongshore forces in Niño conditions (in m s^{-1}) and d) air temperature (in °C). Averages were computed over November 1997-February 1998, between 7°S and 15°S, and within 100 km from the coast. Full and dashed lines in a) and c) correspond to El Niño and mean climatological conditions, respectively.

Figure 12. Same as Figure 11 but for the period July-August 1997.

Figure 13: a) Time series of coastal alongshore wind anomalies (in m s^{-1}) from CRTL (black line), SST-EN (red line), BRY-EN (blue line) experiments. Mean alongshore wind profiles (in m s^{-1}) in b) July-August 1997 and c) November 1997-February 1998. Black-dashed, black, red and blue lines mark the climatological (CLIM) ,CRTL, SST-EN and BRY-EN profiles, respectively.

Figure 14. Mean (red contours) and anomalous (shading) sea level pressure (in hPa) during a) March-September 1997 and b) October 1997–March 1998. White contours mark pressure climatological values (1994-2000).

Figure 15. Anomalies of air humidity at 2 meters (in g kg^{-1}, green line), downward shortwave radiation at sea surface (in W m^{-2}, red line) and land-sea air temperature gradient at 2 meters (in 10^{-2} °C km, blue line). Anomalies of air humidity and shortwave radiation were taken at the model land grid points closest to sea. Temperature gradient was computed as the difference between the model land grid point closest to sea and the sea grid point closest to land at each latitude. All variables were averaged between 7°S and 15°S.

Figure 16. Time evolution of alongshore SST gradient (in °C/80 km, positive equatorward, red line) and alongshore wind (in m s^{-1}, black line) anomalies for ERA-Interim reanalysis over 1979-2016. Anomalies were averaged in a 160-km-wide coastal band and between 7°S and 15°S. Grey vertical bands indicate El Niño periods.

Figure 1

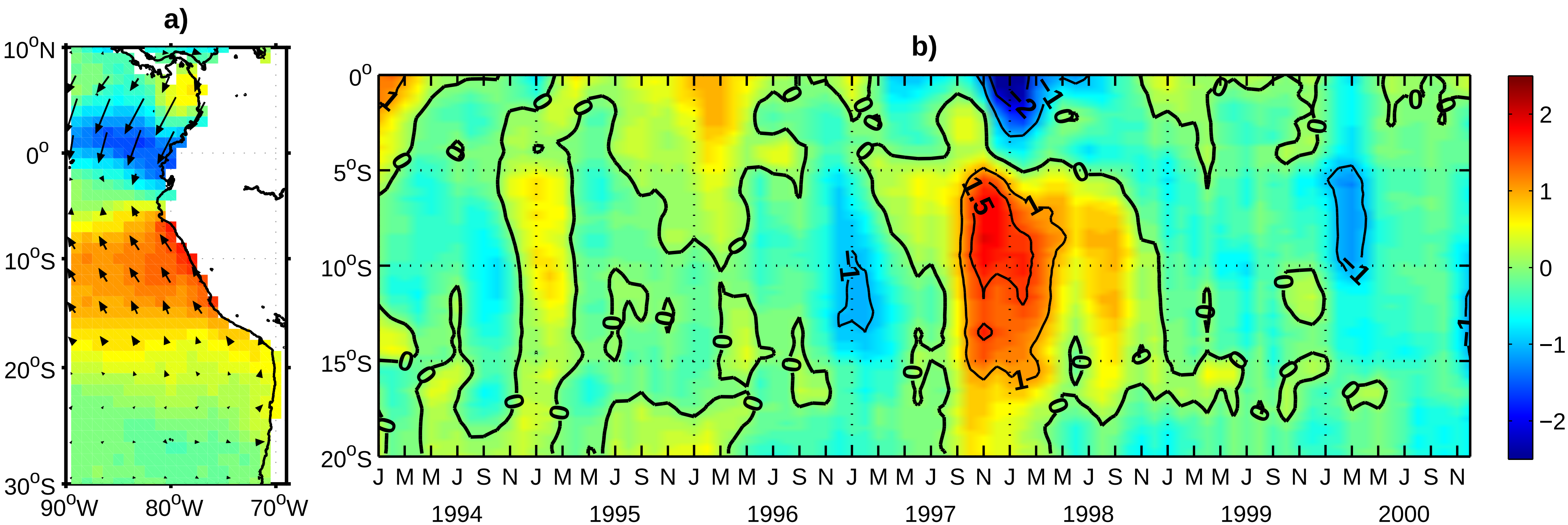

a)
10^{0}N
0^{0}
10^{0}S
20^{0}S
30^{0}S
90^{0}W
80^{0}W
70^{0}W
b)
0^{0}
5^{0}S
10^{0}S
15^{0}S
20^{0}S
J M M J S N J M M J S N J M M J S N J M M J S N J M M J S N J M M J S N J M M J S N
1994
1995
1996
1997
1998
1999
2000
2
1
0
−1
−2

Figure 2

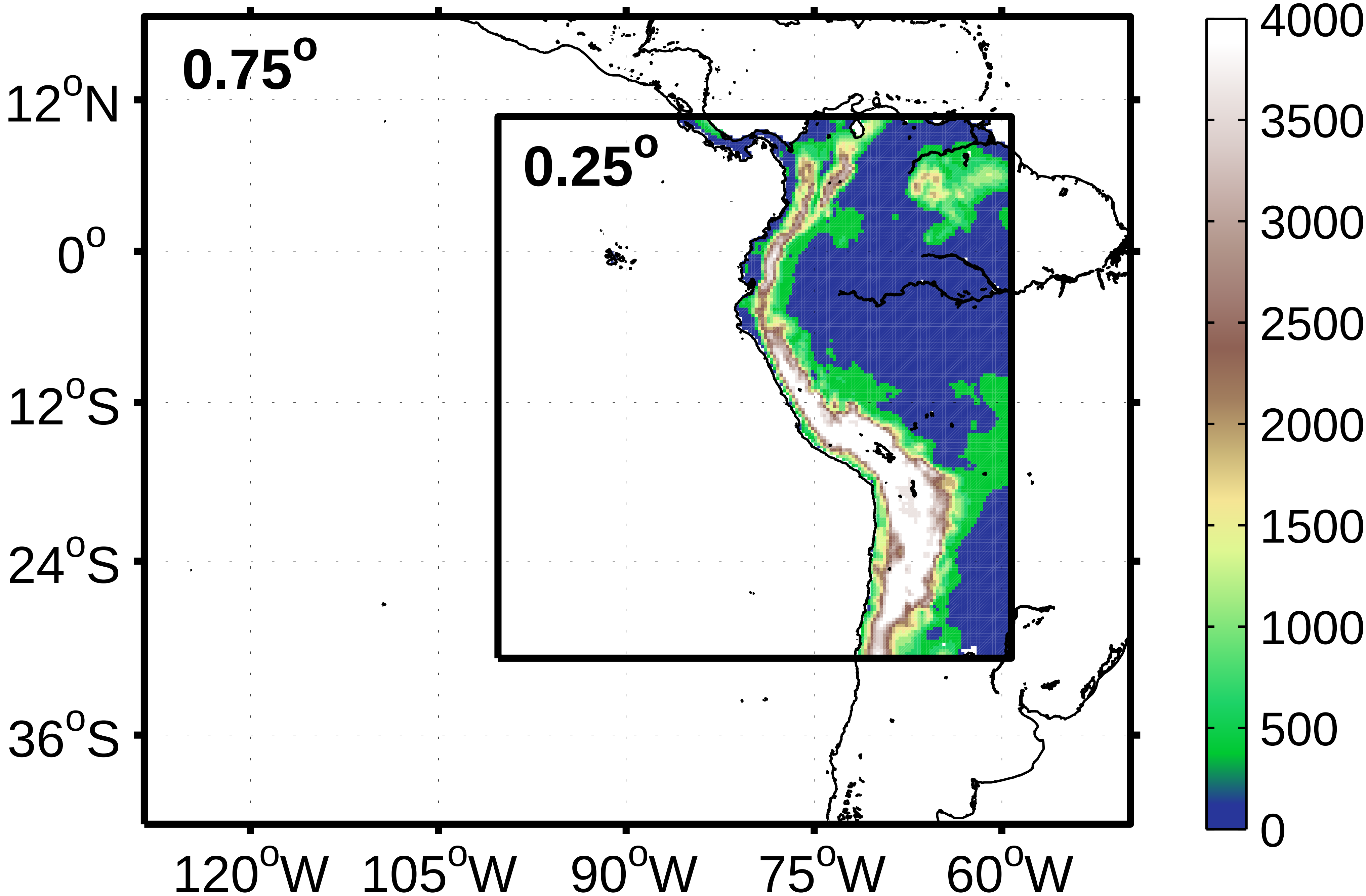

0.75°
0.25°
12°N
0°
12°S
24°S
36°S
120°W
105°W
90°W
75°W
60°W
4000
3500
3000
2500
2000
1500
1000
500
0

Figure 3

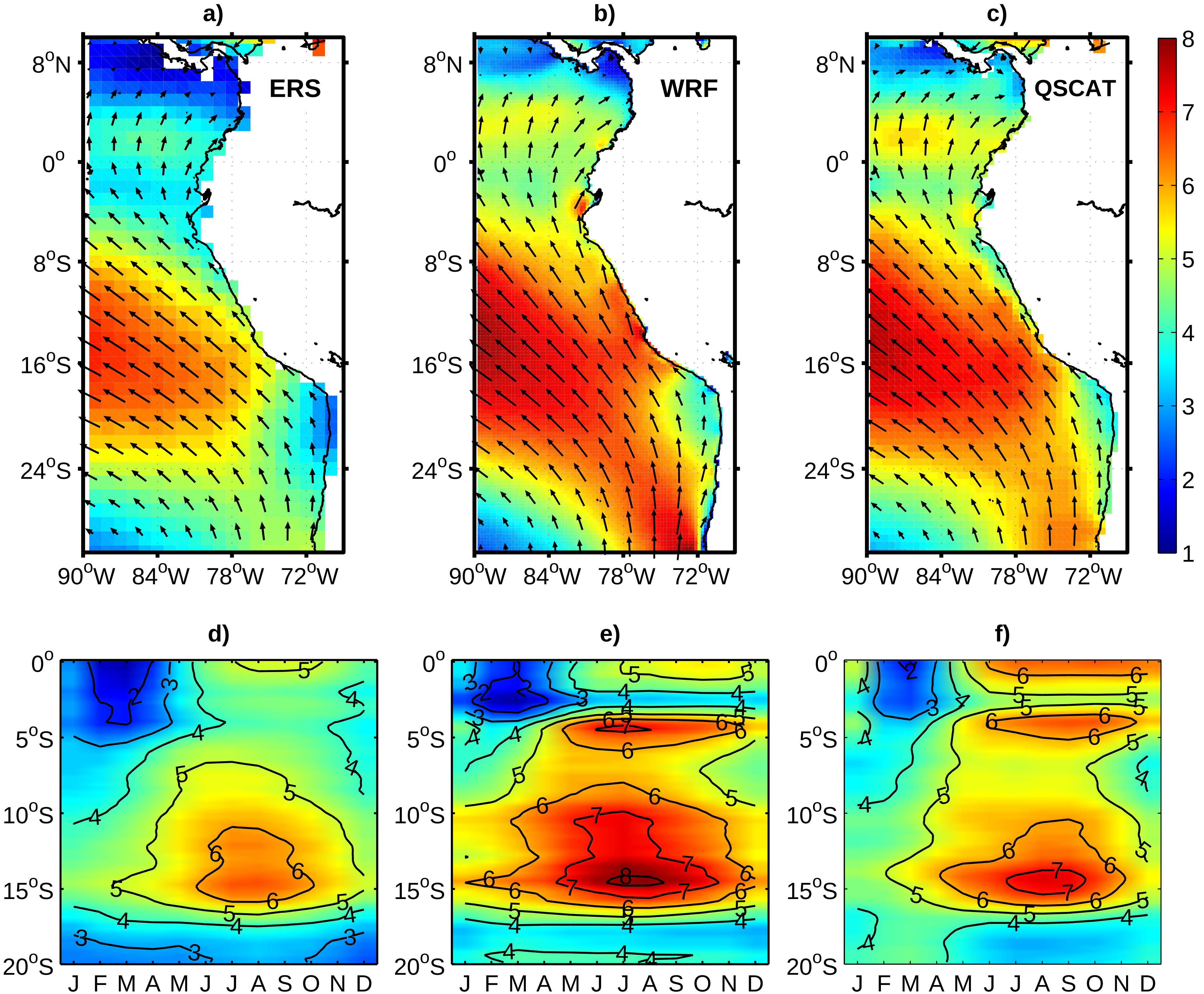

a)
b)
c)
ERS
WRF
QSCAT
8°N
0°
8°S
16°S
24°S
90°W
84°W
78°W
72°W
1
2
3
4
5
6
7
8
d)
e)
f)
0°
5°S
10°S
15°S
20°S
J F M A M J J A S O N D

Figure 4

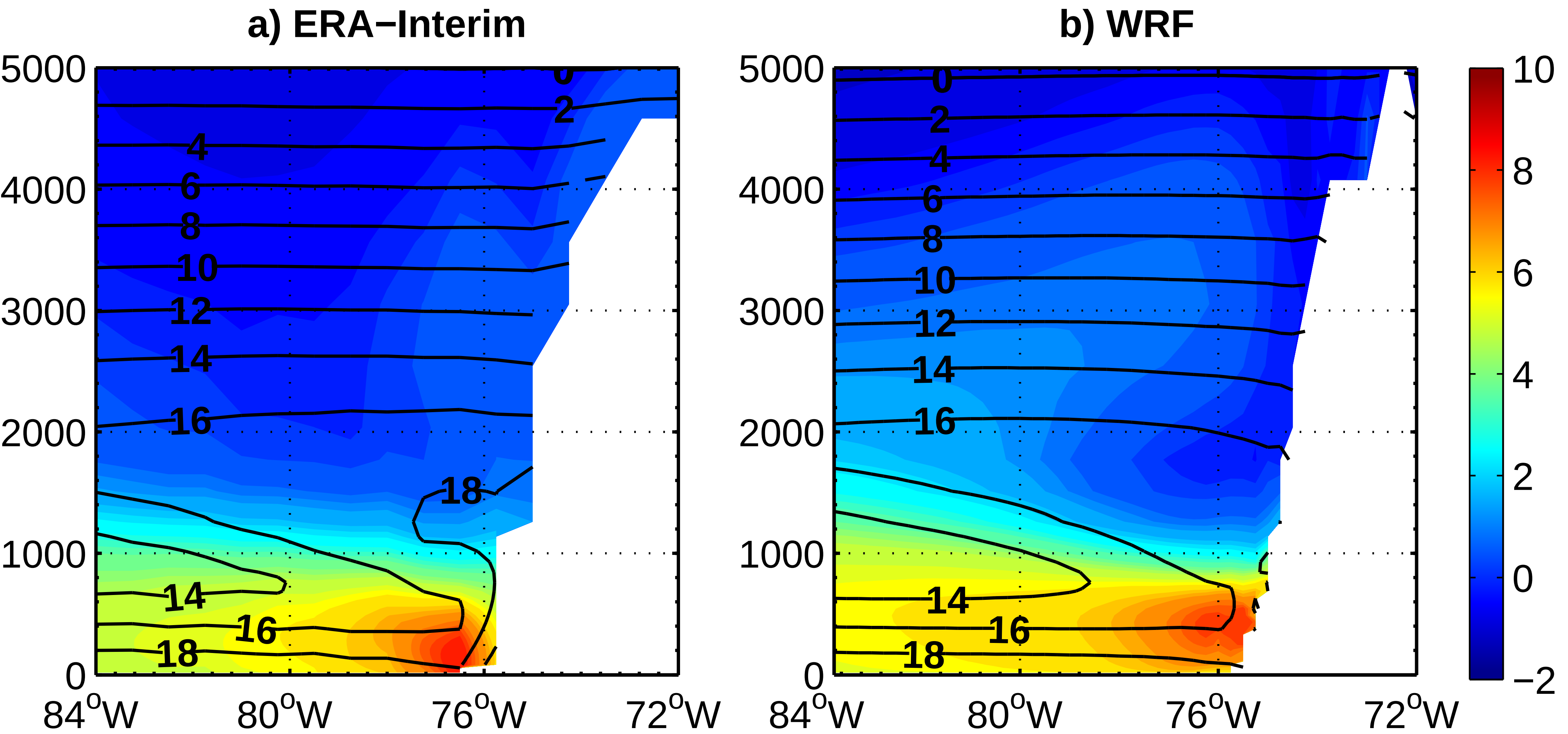

a) ERA−Interim
b) WRF
5000
4000
3000
2000
1000
0
84°W
80°W
76°W
72°W
0
2
4
6
8
10
12
14
16
18
10
8
6
4
2
0
−2

Figure 5

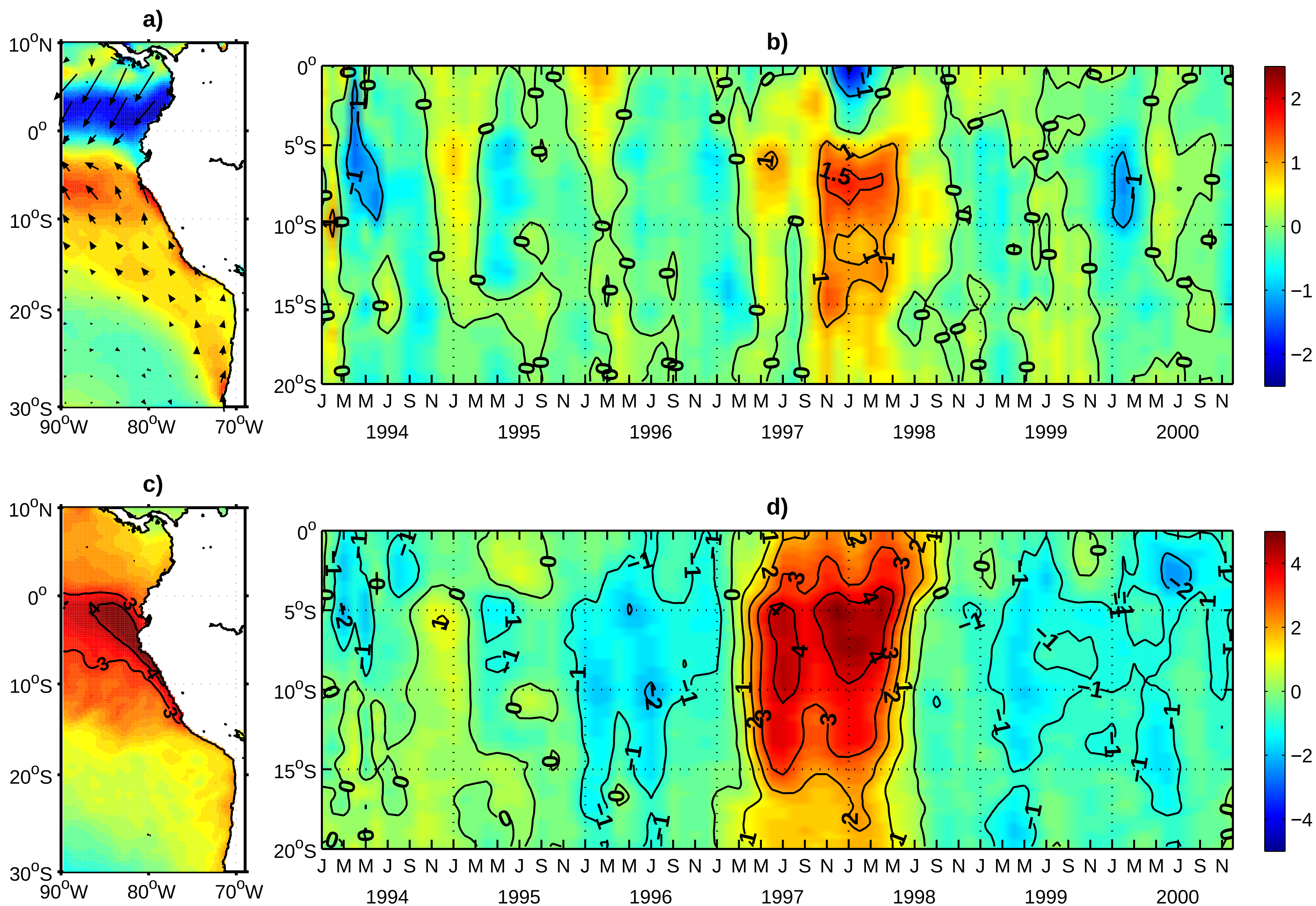
a)
b)
c)
d)
10°N
0°
10°S
20°S
30°S
90°W
80°W
70°W
0°
5°S
10°S
15°S
20°S
J M M J S N J M M J S N J M M J S N J M M J S N J M M J S N J M M J S N J M M J S N
1994
1995
1996
1997
1998
1999
2000
2
1
0
−1
−2
4
2
0
−2
−4

Figure 6

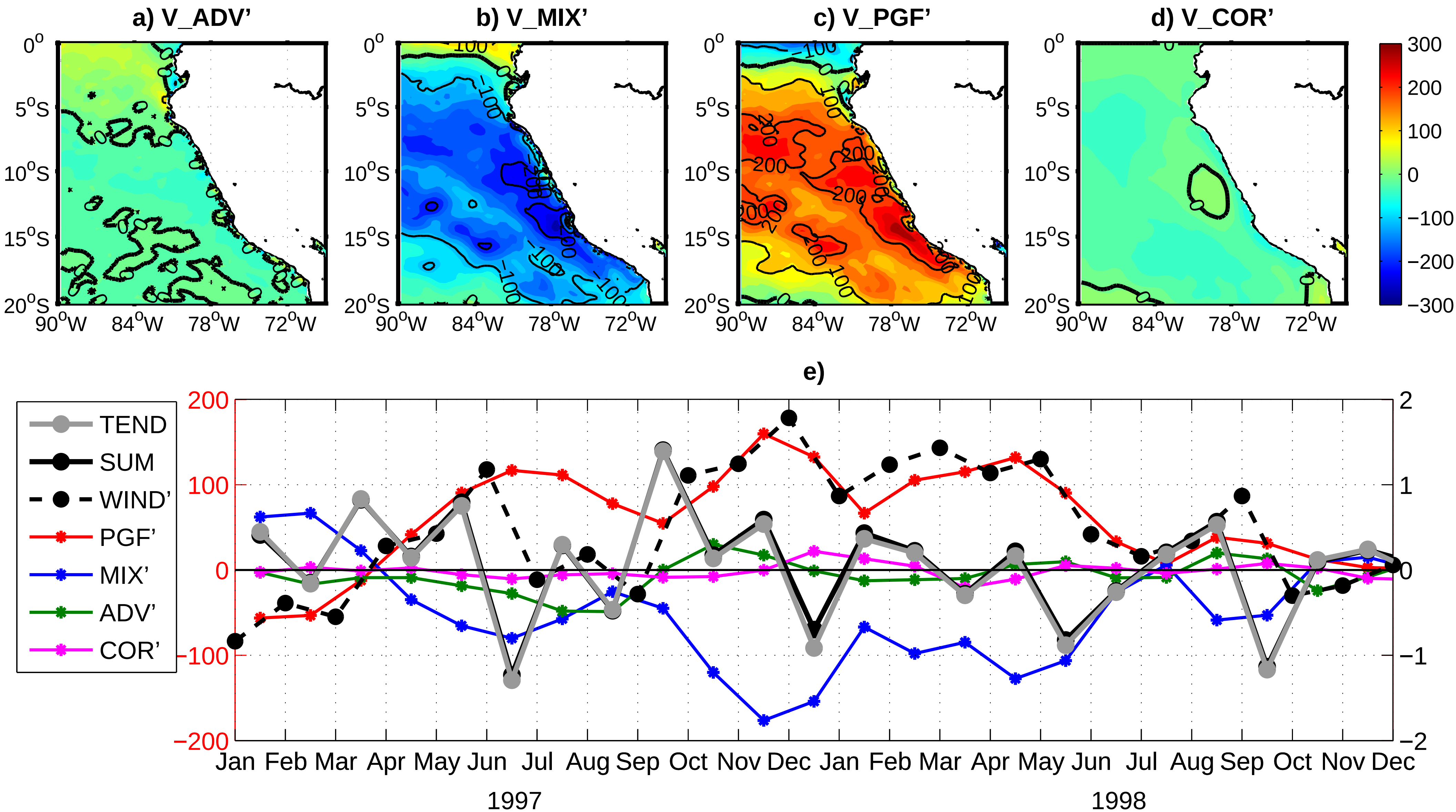

a) V_ADV'
b) V_MIX'
c) V_PGF'
d) V_COR'
0°
5°S
10°S
15°S
20°S
90°W
84°W
78°W
72°W
300
200
100
0
−100
−200
−300
e)
TEND
SUM
WIND'
PGF'
MIX'
ADV'
COR'
200
100
0
−100
−200
2
1
0
−1
−2
Jan Feb Mar Apr May Jun Jul Aug Sep Oct Nov Dec Jan Feb Mar Apr May Jun Jul Aug Sep Oct Nov Dec
1997
1998

Figure 7

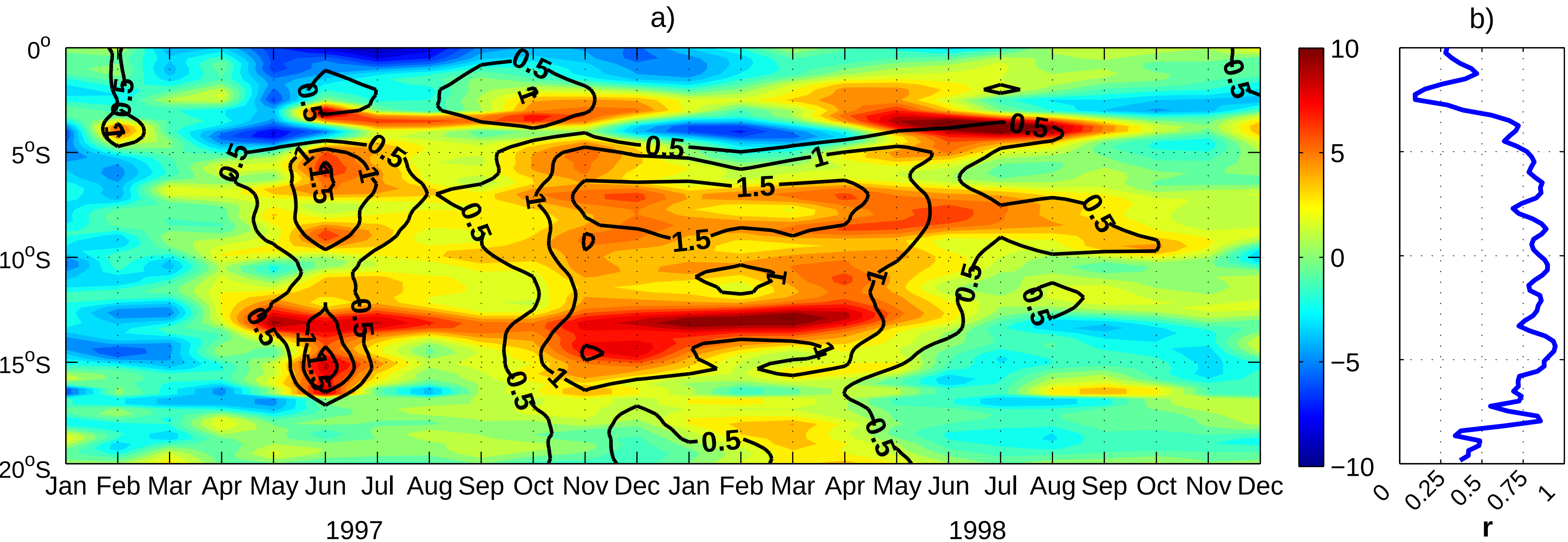

a)
b)
0°
5°S
10°S
15°S
20°S
Jan Feb Mar Apr May Jun Jul Aug Sep Oct Nov Dec Jan Feb Mar Apr May Jun Jul Aug Sep Oct Nov Dec
1997
1998
10
5
0
−5
−10
0
0.25
0.5
0.75
1
r

Figure 8

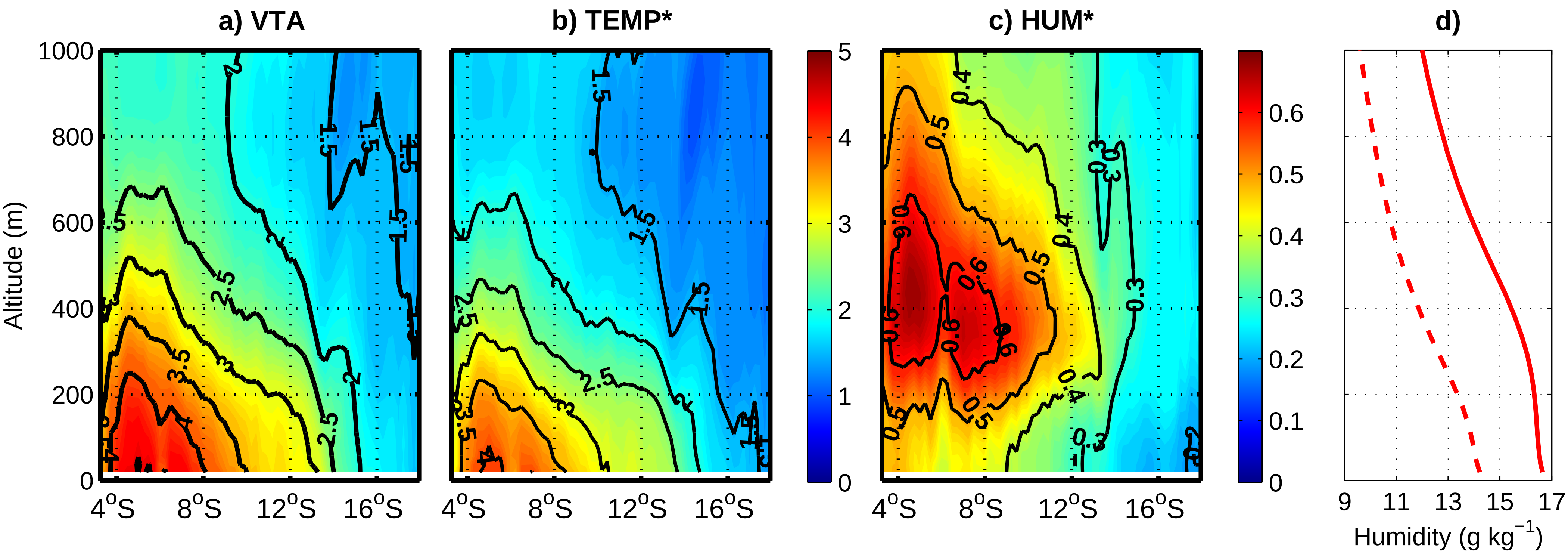
a) VTA
b) TEMP*
c) HUM*
d)
Altitude (m)
1000
800
600
400
200
0
4°S
8°S
12°S
16°S
5
4
3
2
1
0
0.6
0.5
0.4
0.3
0.2
0.1
0
9
11
13
15
17
Humidity (g kg⁻¹)

Figure 9

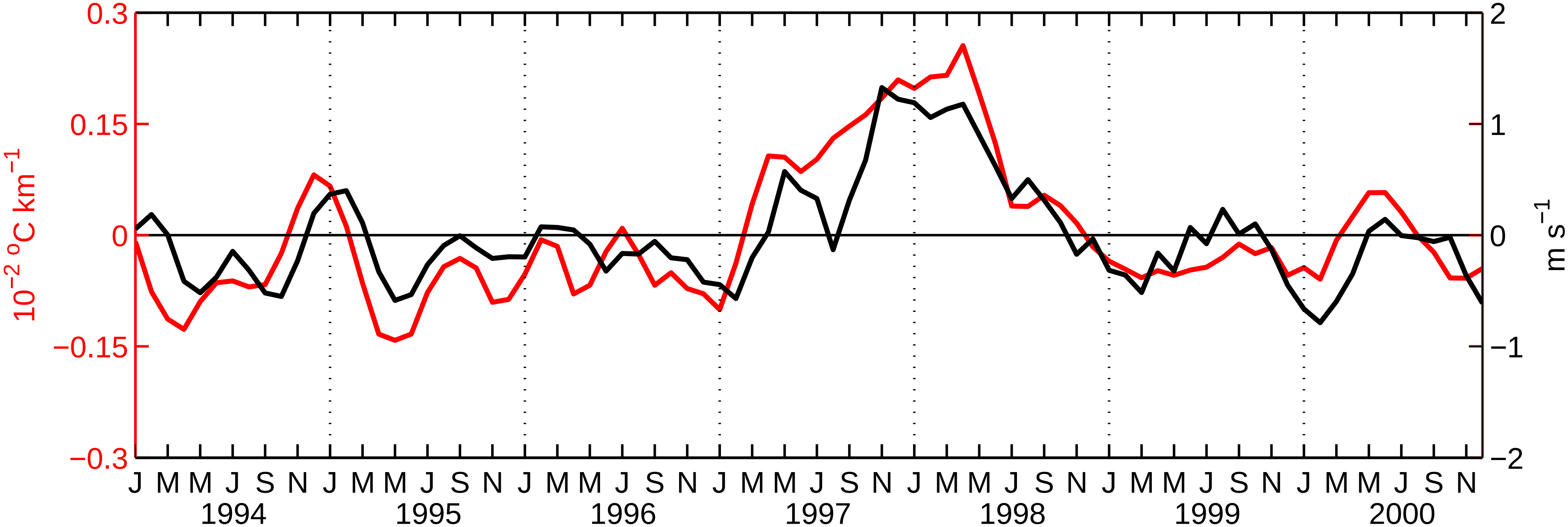
0.3
0.15
0
−0.15
−0.3
10^{-2} ^{o}C km^{-1}
2
1
0
−1
−2
m s^{-1}
J M M J S N J M M J S N J M M J S N J M M J S N J M M J S N J M M J S N J M M J S N
1994
1995
1996
1997
1998
1999
2000

Figure 10

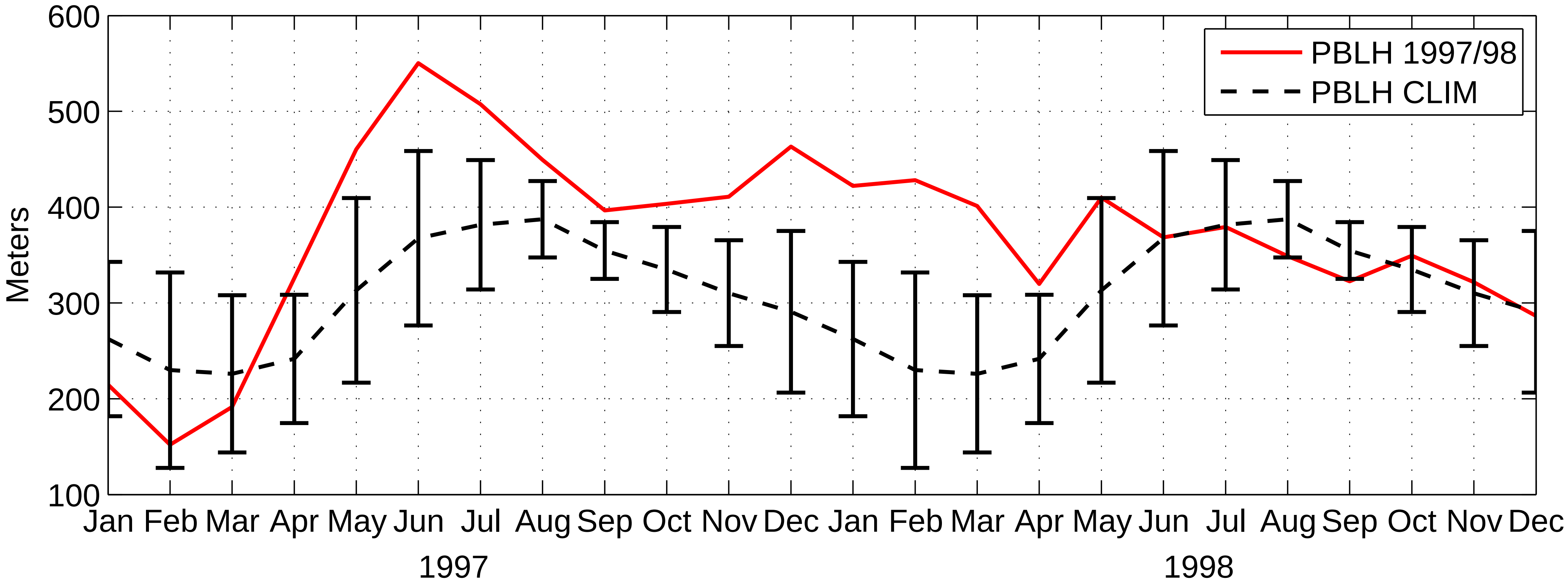
PBLH 1997/98
PBLH CLIM
Meters
600
500
400
300
200
100
Jan Feb Mar Apr May Jun Jul Aug Sep Oct Nov Dec Jan Feb Mar Apr May Jun Jul Aug Sep Oct Nov Dec
1997
1998

Figure 11

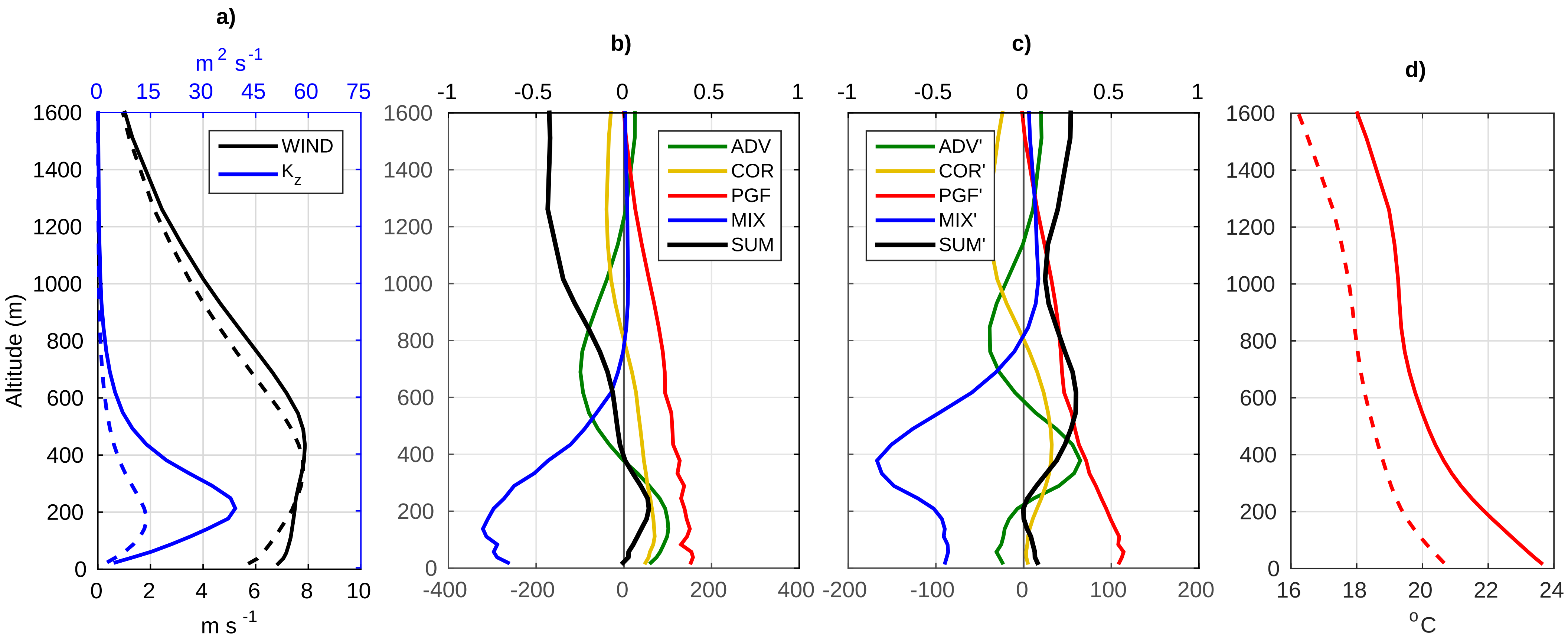

a)
m 2 s -1
0 15 30 45 60 75
WIND
K z
Altitude (m)
0 200 400 600 800 1000 1200 1400 1600
0 2 4 6 8 10
m s -1
b)
-1 -0.5 0 0.5 1
ADV
COR
PGF
MIX
SUM
-400 -200 0 200 400
c)
ADV'
COR'
PGF'
MIX'
SUM'
-200 -100 0 100 200
d)
16 18 20 22 24
oC

Figure 12

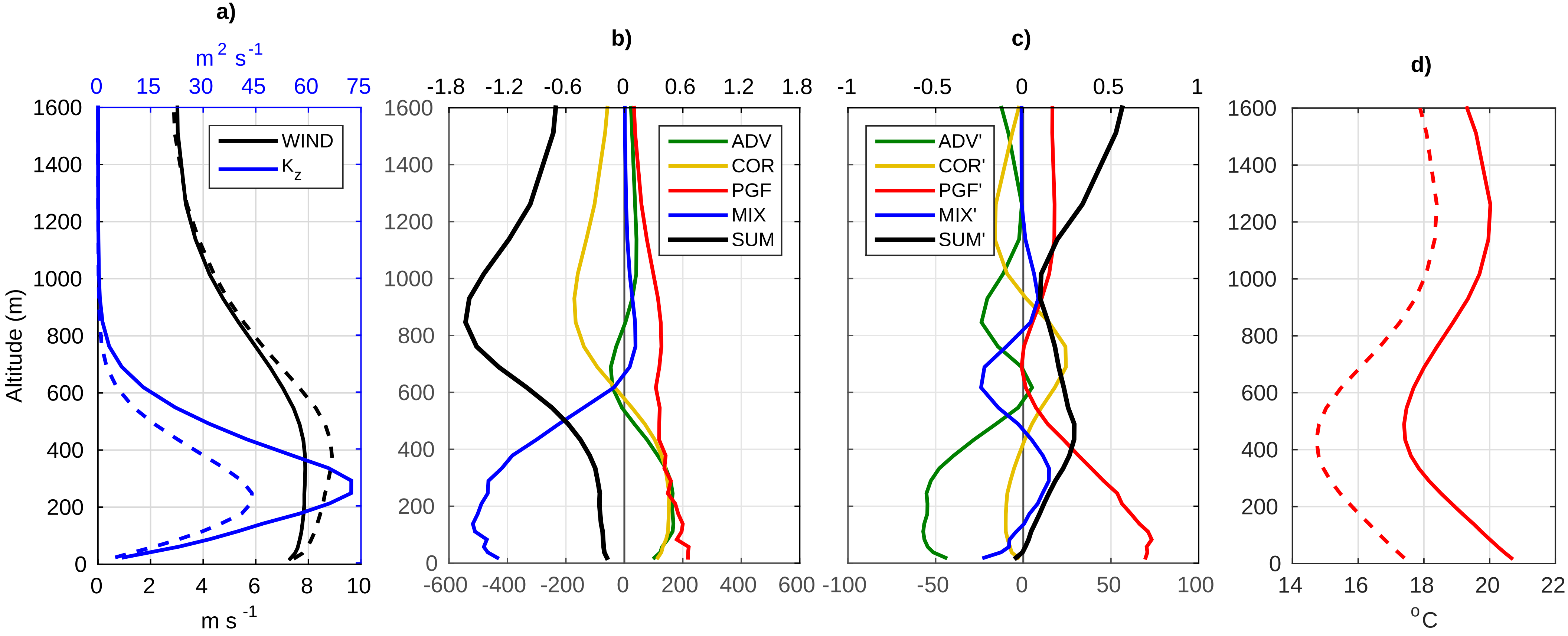

a)
m 2 s -1
0 15 30 45 60 75
WIND
Kz
Altitude (m)
m s -1
b)
ADV
COR
PGF
MIX
SUM
c)
ADV'
COR'
PGF'
MIX'
SUM'
d)
oC

Figure 13

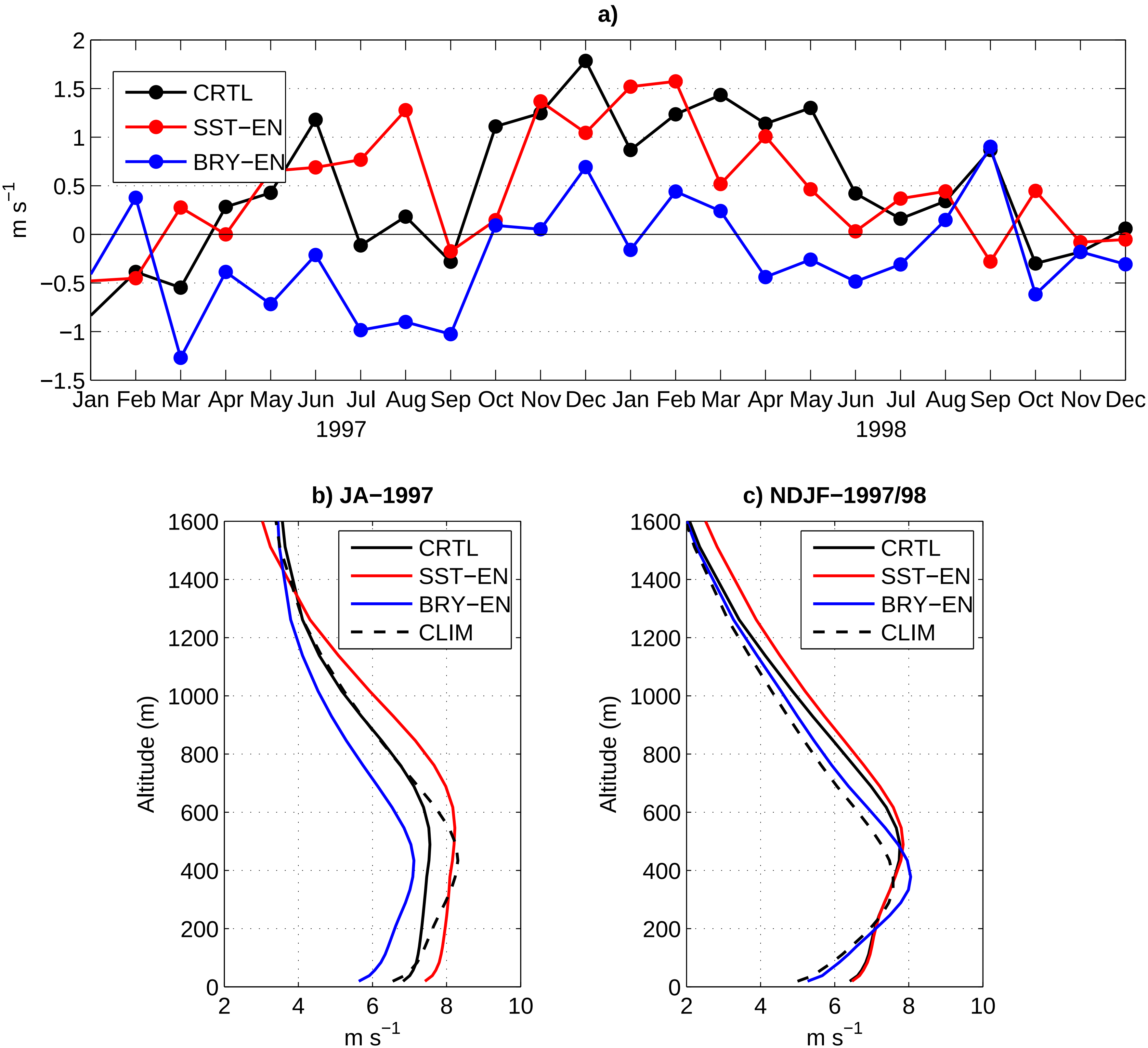
a)
CRTL
SST−EN
BRY−EN
m s−1
2
1.5
1
0.5
0
−0.5
−1
−1.5
Jan Feb Mar Apr May Jun Jul Aug Sep Oct Nov Dec Jan Feb Mar Apr May Jun Jul Aug Sep Oct Nov Dec
1997
1998
b) JA−1997
c) NDJF−1997/98
CRTL
SST−EN
BRY−EN
CLIM
Altitude (m)
1600
1400
1200
1000
800
600
400
200
0
2
4
6
8
10
m s−1

Figure 14

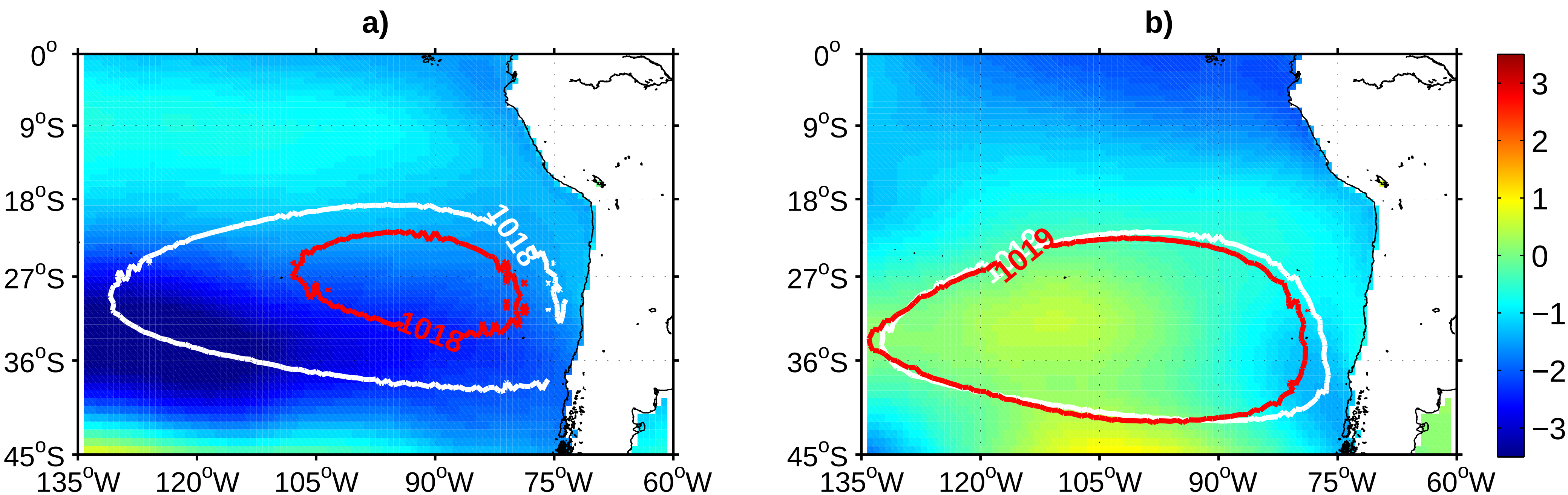

a)
b)
0°
9°S
18°S
27°S
36°S
45°S
135°W
120°W
105°W
90°W
75°W
60°W
1018
1018
1019
3
2
1
0
−1
−2
−3

Figure 15

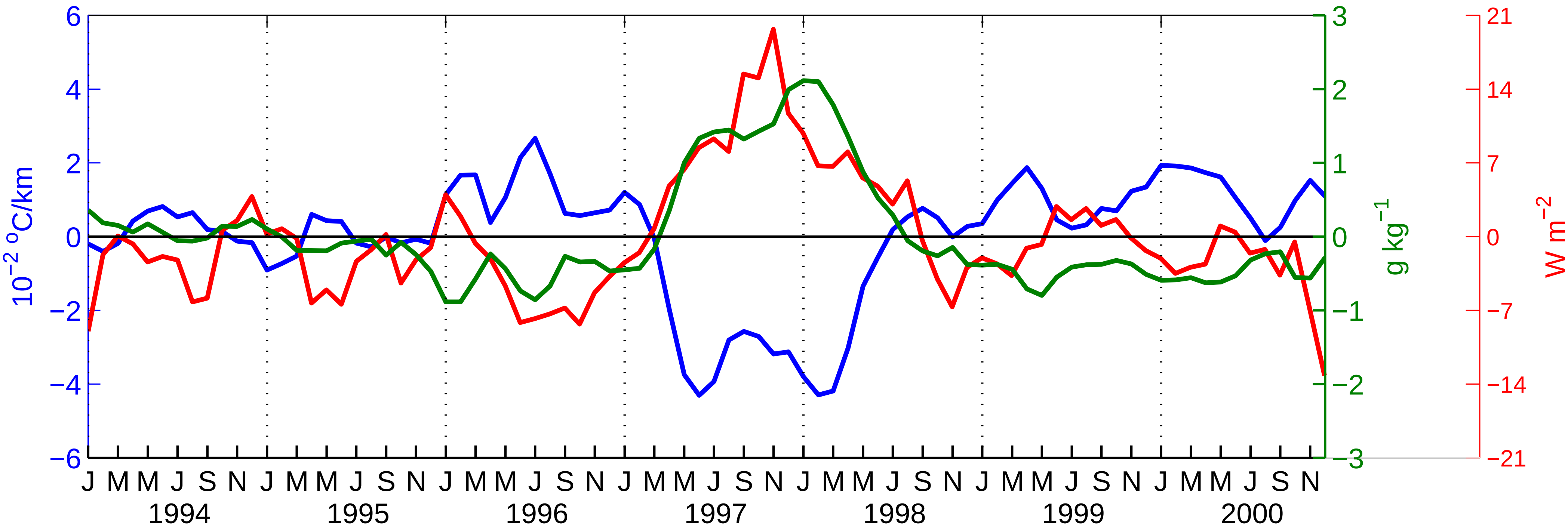
6
4
2
0
−2
−4
−6
10^{-2} ^oC/km
3
2
1
0
−1
−2
−3
g kg^{-1}
21
14
7
0
−7
−14
−21
W m^{-2}
J M M J S N J M M J S N J M M J S N J M M J S N J M M J S N J M M J S N J M M J S N
1994
1995
1996
1997
1998
1999
2000

Figure 16

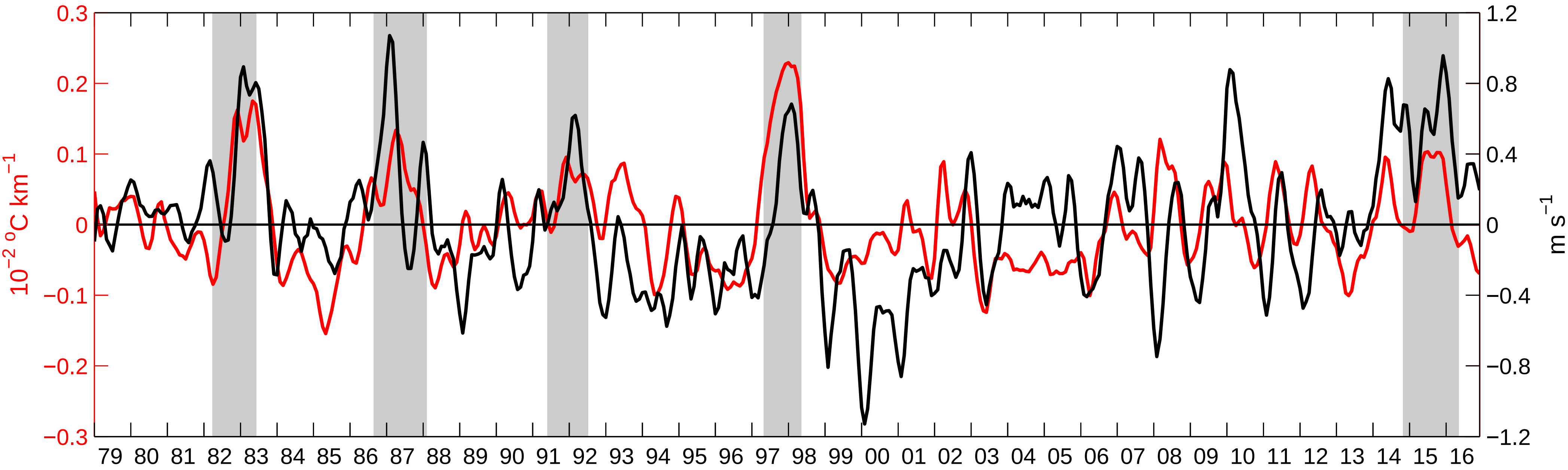

0.3
0.2
0.1
0
−0.1
−0.2
−0.3
10^{-2} °C km^{-1}
1.2
0.8
0.4
0
−0.4
−0.8
−1.2
m s^{-1}
79 80 81 82 83 84 85 86 87 88 89 90 91 92 93 94 95 96 97 98 99 00 01 02 03 04 05 06 07 08 09 10 11 12 13 14 15 16

Table 1. Parameterizations used in WRF model for the simulations.

Processes	Scheme	Reference
Shortwave Radiation	Dudhia scheme	Dudhia (1989)
Longwave Radiation	RRTM scheme	Mlawer et al. (1997)
Microphysics	WRF Single-Moment 6-class scheme	Hong and Lim (2006)
Cumulus	Betts-Miller-Janjic scheme	Janjic (1994)
Surface Layer	MYNN surface layer	Nakanishi and Niino (2009)
Land Surface	Noah Land Surface Model	Chen and Dudhia (2001)
Planetary Boundary Layer	MYNN Level 2.5 PBL	Nakanishi and Niino (2009)